OPEN ACCESS



Early Planet Formation in Embedded Disks (eDisk). IX. High-resolution ALMA Observations of the Class 0 Protostar R CrA IRS5N and Its Surroundings

Rajeeb Sharma ¹, Jes K. Jørgensen ¹, Sacha Gavino ¹, Nagayoshi Ohashi ², John J. Tobin ³, Zhe-Yu Daniel Lin ⁴, Zhi-Yun Li⁴, Shigehisa Takakuwa^{2,5}, Chang Won Lee^{6,7}, Jinshi Sai (Insa Choi)², Woojin Kwon^{8,9}, Itziar de Gregorio-Monsalvo¹⁰, Alejandro Santamaría-Miranda¹⁰, Hsi-Wei Yen², Yuri Aikawa¹¹, Yusuka Aso⁶, Shih-Ping Lai^{2,12,13,14}, Jeong-Eun Lee¹⁵, Leslie W. Looney¹⁶, Nguyen Thi Phuong^{6,17}, Travis J. Thieme^{12,13,14}, and Jonathan P. Williams 18 (1) ¹ Niels Bohr Institute, University of Copenhagen, Øster Voldgade 5-7, DK-1350, Copenhagen K, Denmark; rajeeb.sharma@nbi.ku.dk ² Academia Sinica Institute of Astronomy& Astrophysics 11F of Astronomy-Mathematics Building, AS/NTU, No.1, Sec. 4, Roosevelt Rd, Taipei 10617, Taiwan, R.O.C ³ National Radio Astronomy Observatory, 520 Edgemont Rd., Charlottesville, VA 22903, USA University of Virginia, 530 McCormick Rd., Charlottesville, VA 22903, USA ⁵ Department of Physics and Astronomy, Graduate School of Science and Engineering, Kagoshima University, 1-21-35 Korimoto, Kagoshima, Kagoshima 890-0065, Japan ⁶ Korea Astronomy and Space Science Institute, 776 Daedeok-daero Yuseong-gu, Daejeon 34055, Republic of Korea University of Science and Technology, 217 Gajeong-ro Yuseong-gu, Daejeon 34113, Republic of Korea ⁸ Department of Earth Science Education, Seoul National University, 1 Gwanak-ro, Gwanak-gu, Seoul 08826, Republic of Korea SNU Astronomy Research Center, Seoul National University, I Gwanak-ro, Gwanak-gu, Seoul 08826, Republic of Korea European Southern Observatory, Alonso de Cordova 3107, Casilla 19, Vitacura, Santiago, Chile Department of Astronomy, Graduate School of Science, The University of Tokyo, 7-3-1 Hongo, Bunkyo-ku, Tokyo 113-0033, Japan Institute of Astronomy, National Tsing Hua University, No. 101, Sec. 2, Kuang-Fu Rd., Hsinchu 30013, Taiwan ¹³ Center for Informatics and Computation in Astronomy, National Tsing Hua University, No. 101, Sec. 2, Kuang-Fu Rd., Hsinchu 30013, Taiwan Department of Physics, National Tsing Hua University, No. 101, Sec. 2, Kuang-Fu Rd., Hsinchu 30013, Taiwan Department of Physics and Astronomy, Seoul National University, 1 Gwanak-ro, Gwanak-gu, Seoul 08826, Republic of Korea

16 Department of Astronomy, University of Illinois, 1002 West Green St., Urbana, IL 61801, USA ¹⁷ Department of Astrophysics, Vietnam National Space Center, Vietnam Academy of Science and Technology, 18 Hoang Quoc Viet, Cau Giay, Hanoi, Vietnam Institute for Astronomy, University of Hawai'i at Mānoa, 2680 Woodlawn Dr., Honolulu, HI 96822, USA Received 2023 April 27; revised 2023 June 30; accepted 2023 July 1; published 2023 August 23

Abstract

We present high-resolution high-sensitivity observations of the Class 0 protostar RCrA IRS5N as part of the Atacama Large Milimeter/submilimeter Array large program Early Planet Formation in Embedded Disks. The 1.3 mm continuum emission reveals a flattened continuum structure around IRS5N, consistent with a protostellar disk in the early phases of evolution. The continuum emission appears smooth and shows no substructures. However, a brightness asymmetry is observed along the minor axis of the disk, suggesting that the disk is optically and geometrically thick. We estimate the disk mass to be between 0.007 and 0.02 M_{\odot} . Furthermore, molecular emission has been detected from various species, including $C^{18}O(2-1)$, $^{12}CO(2-1)$, $^{13}CO(2-1)$, and $H_2CO(3_{0,3}-2_{0,2},\ 3_{2,1}-2_{2,0})$, and $3_{2,2}-2_{2,1})$. By conducting a position-velocity analysis of the $C^{18}O(2-1)$ emission, we find that the disk of IRS5N exhibits characteristics consistent with Keplerian rotation around a central protostar with a mass of approximately $0.3\ M_{\odot}$. Additionally, we observe dust continuum emission from the nearby binary source IRS5a/b. The emission in ^{12}CO toward IRS5a/b seems to emanate from IRS5b and flow into IRS5a, suggesting material transport between their mutual orbits. The lack of a detected outflow and large-scale negatives in ^{12}CO observed toward IRS5N suggests that much of the flux from IRS5N is being resolved out. Using a 1D radiative transfer model, we infer the mass of the envelope surrounding IRS5N to be $\sim 1.2\ M_{\odot}$. Due to this substantial surrounding envelope, the central IRS5N protostar is expected to be significantly more massive in the future.

Unified Astronomy Thesaurus concepts: Protostars (1302); Young stellar objects (1834); Protoplanetary disks (1300); Interstellar medium (847)

1. Introduction

Protostellar disks form as an outcome of the conservation of angular momentum during the gravitational collapse of the dust and gas in the envelope surrounding young stars (e.g., Terebey et al. 1984; McKee & Ostriker 2007). These disks not only regulate the mass accreted onto the protostar, but also provide the necessary ingredients for planet formation (Testi et al. 2014). Recent Atacama Large Milimeter/submilimeter Array (ALMA)

Original content from this work may be used under the terms of the Creative Commons Attribution 4.0 licence. Any further distribution of this work must maintain attribution to the author(s) and the title of the work, journal citation and DOI.

observations with high spatial resolution have discovered that substructures such as gaps and rings are common in the dust emission of Class II young stellar object disks (ALMA Partnership et al. 2015; Andrews et al. 2018; Cieza et al. 2021). While these structures can be attributed to features such as snowlines and dust traps (Zhang et al. 2015; Gonzalez et al. 2017), they are largely thought to be indications of embedded planets (Dong et al. 2015; Zhang et al. 2018). The direct imaging of possible protoplanets in the gap of the continuum emission of the protostar PDS 70 further supports this idea (Keppler et al. 2018; Isella et al. 2019; Benisty et al. 2021).

Recent studies have shown that the mass reservoir of Class II disks is generally insufficient to form giant planets

(Tychoniec et al. 2020). This suggests that planet formation is already well underway by the time a protostar reaches the Class II (T Tauri) phase. Interferometric observations over the last decade have shown that protostellar disks can be found in younger Class 0/I protostars (e.g., Tobin et al. 2012, 2020; Brinch & Jørgensen 2013; Ohashi et al. 2014; Sheehan & Eisner 2017; Sharma et al. 2020). These disks are generally found to be larger and possibly more turbulent compared to disks around more evolved sources (Sheehan & Eisner 2017; Tychoniec et al. 2020). Furthermore, evidence of substructures has been observed in a handful of embedded Class I sources (e.g., Sheehan & Eisner 2017; Segura-Cox et al. 2020; Sheehan et al. 2020). These results, combined with the ubiquity of substructures in Class II disks, suggest that planet formation likely begins earlier during the Class 0/I phase when the disk is still embedded in its natal envelope.

To constrain how and when substructures form in young (≤1 Myr old) protostellar disks and ultimately understand their nature, a sample of 19 nearby Class 0/I protostellar systems has been studied with ALMA as part of the Large Program Early Planet Formation in Embedded Disks (eDisk; Ohashi et al. 2023). One of these deeply embedded protostars located in the R Coronae Australis (R CrA) region, the most active star formation region in the Corona Australis molecular cloud, is the Class 0 source RCrA IRS5N (hereafter IRS5N; Harju et al. 1993; Chini et al. 2003). IRS5N (also referred to as CrA-20; Peterson 2011) is part of a group of a dozen deeply embedded young stellar objects (YSOs) in a cluster dubbed the Coronet in the R CrA region (Taylor & Storey 1984). Traditionally, the cluster is estimated to be at a distance of \sim 130 pc. However, from the recent Gaia DR2 parallax measurements, the distance to the cluster has been updated to 147 ± 5 pc (Zucker et al. 2020), which we have adopted for this paper. This value is consistent with the distance of 149.4 ± 0.4 pc measured recently by Galli et al. (2020).

The Coronet has been extensively observed from X-rays to radio wavelengths (e.g., Peterson 2011; Lindberg et al. 2014; Sandell et al. 2021; see also the review by Neuhäuser & Forbrich 2008). Based on Spitzer photometry of the Coronet, IRS5N was first classified as a Class I source (Peterson 2011), which was later updated to Class 0 with the addition of Herschel and JCMT/SCUBA data (Lindberg et al. 2014). From a recent reanalysis of the spectral energy distribution (SED) of IRS5N using the most recent photometry and the updated Gaia distance above, we find a bolometric temperature $(T_{bol}) = 59 \text{ K}$ and a bolometric luminosity $(L_{bol}) = 1.40 L_{\odot}$ (Ohashi et al. 2023). The highest angular resolution observations of IRS5N at submillimeter wavelengths so far were from the Submillimeter Array (SMA) in the compact configuration at a resolution of 4.6×2.6 (Peterson 2011). In this paper, part of the series of first-look papers from eDisk, we present the first high angular resolution (\sim 0."05) high-sensitivity continuum and spectral line observations toward IRS5N using ALMA. The field of view of our ALMA observations of IRS5N also captures the nearby binary protostar, IRS5 a and b. IRS5 (also known as R CrA 19; Peterson 2011) was first reported in Taylor & Storey (1984) and was later found to be a binary (Chen & Graham 1993; Nisini et al. 2005).

The paper is structured as follows: The observations and the data reduction process are described in Section 2. The empirical results from the observations of the disk continuum and the molecular line emission are presented in Section 3. The

implications of the results are discussed in Section 4, and the conclusions are presented in Section 5.

2. Observations and Data Reduction

IRS5N was observed as part of the eDisk ALMA large program (2019.1.00261.L, PI: N. Ohashi) in Band 6 at 1.3 mm wavelength. The short-baseline observations were conducted on 2021 May 4 and on 2021 May 15 for a total on-source time of \sim 76 minutes. The long-baseline observations were made between 2021 August 18 and October 2 for a total on-source time of \sim 256 minutes. The shortest and longest projected baselines were 15 m and 11,615 m, respectively. Along with the continuum, molecular line emissions from 12 CO, 13 CO, 13 CO, SO, SiO, DCN, c C- 3 H₂, H₂CO, CH₃OH, and DCN were also targeted. A detailed description of the observations along with the spectral setup, correlator setup, and calibration is provided in Ohashi et al. (2023).

The ALMA pipeline-calibrated long- and short-baseline data were further reduced and imaged using the Common Astronomy Software Application (CASA) 6.2.1 (McMullin et al. 2007). The source position was estimated by calculating the continuum peak position for each execution block and aligned to a single phase center when calculating the scaling between the execution blocks. The self-calibration was carried out using the native phase centers of the observations. The short-baseline data were initially self-calibrated with six rounds of phase-only calibration, followed by three rounds of phase and amplitude calibration. Then, the long-baseline data were combined with the self-calibrated short-baseline data, and four more rounds of phase-only calibration were performed on the combined data. The solutions of the continuum self-calibration are applied to the spectral line data as well.

The final continuum images were created with a range of robust parameters from -2.0 to 2.0. We adopt the robust value of 0.5 for the continuum image in this paper, providing a balance between sensitivity and resolution. This resulted in a synthesized beam of 0.052×0.035 and an rms noise of $16~\mu$ Jy beam⁻¹. The spectral line images are created with robust parameters of 0.5 and 2.0 with $uvtaper = 2000 \text{ k}\lambda$. We adopt robust 0.5 for most of the spectral lines, except for the 1.000 and 1.000 lines, where we adopt robust 1.000 to increase the signal-to-noise ratio. The details of the continuum observations and the detected spectral lines are summarized in Table 1.000

3. Results

3.1. Dust Continuum Emission

Figure 1 shows the continuum images from the ALMA data at 1.3 mm. Figure 1(a) displays the large-scale view of the continuum emission from the region, and the remaining panels show the zoom-in of the IRS5N and IRS5 protostars.

Figure 1(b) shows the zoomed-in view of the IRS5N continuum image. The image shows a well-resolved flattened dust structure, which likely traces the disk surrounding the central protostar. The brightest emission of the disk is concentrated at its geometrical center with a peak intensity of 5.53 mJy beam⁻¹ as measured from the emission map, corresponding to a brightness temperature of \sim 94 K, calculated with the full Planck function. The brightness temperature of 94 K is relatively high for a protostar with $L_{\rm bol}=1.4~L_{\odot}$ and deviates from the traditional assumptions of protostars

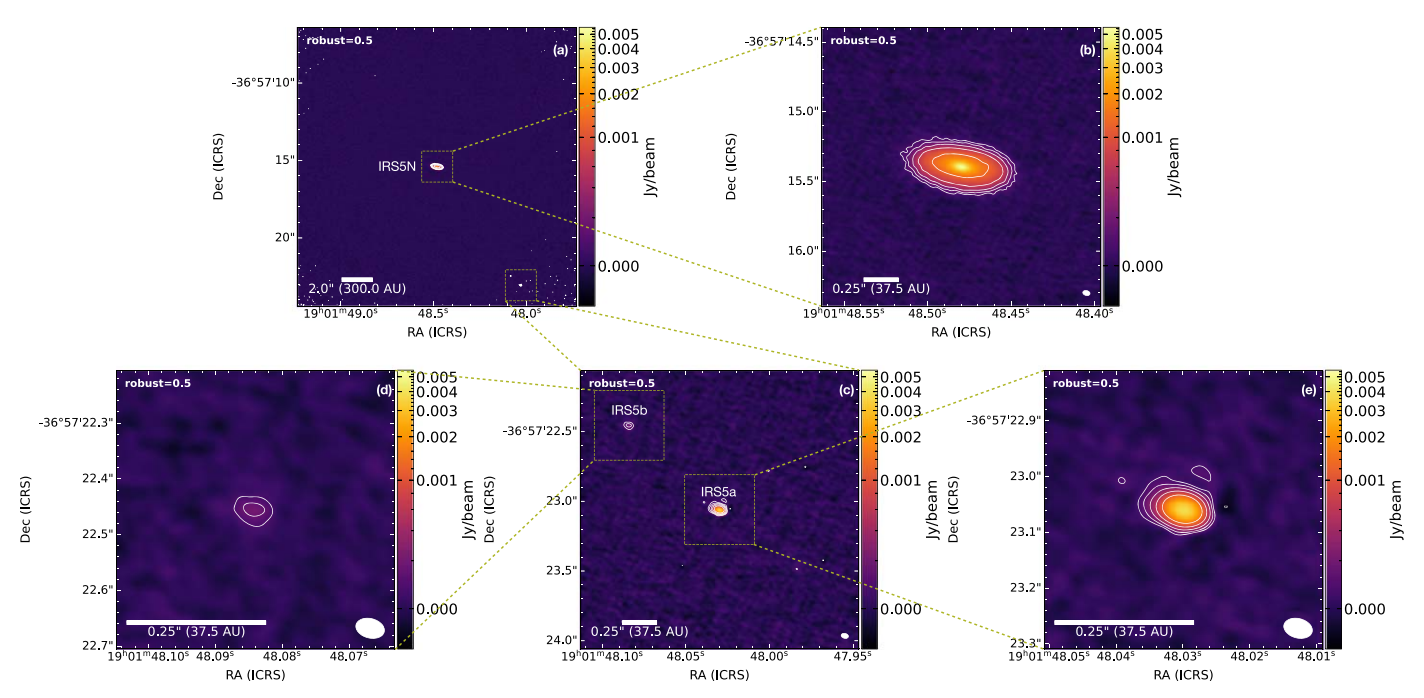


Figure 1. (a) 1.3 mm continuum images of R CrA IRS5N and IRS5 sources with a robust paramater of 0.5. (b) Zoomed-in view of the IRS5N disk. (c) Zoomed-in view of IRS5a and its companion IRS5b. (d) and (e) show further zoomed-in views of the individual sources of the IRS5 binary. The contour levels are 5σ , 10σ , 20σ , 40σ , and 80σ with $\sigma = 0.016$ mJy beam⁻¹. The synthesized beam is shown in white in the bottom right corner with a beam size of $0\rlap.{''}052 \times 0\rlap.{''}035$ and a position angle of $75\rlap.{''}4$. The color stretch used for the images is arcsinh to cover the dynamic range between the sources.

Table 1
Overview of the Continuum and the Detected Molecular Lines

Continuum/Molecules	Transition	Robust	Frequency (GHz)	Beam (")	P.A. (°)	$\frac{\Delta v}{(\text{km s}^{-1})}$	Rms (mJy beam ⁻¹)
Continuum		0.5	225.000000	0.05×0.03	60	•••	0.016
$C^{18}O$	J = 2-1	0.5	219.560354	0.11×0.08	83.8	0.167	1.636
¹² CO	J = 2-1	0.5	230.538000	0.11×0.08	85.9	0.635	0.987
¹³ CO	J = 2-1	2.0	220.398684	0.15×0.11	-87.3	0.167	2.104
H ₂ CO	$J_{K_a,K_c} = 3_{0.3} - 2_{0.2}$	2.0	218.222192	0.14×0.11	-86.6	1.34	0.499
H_2CO	$J_{K_a,K_c} = 3_{2,1} - 2_{2,0}$	2.0	218.760066	0.15×0.11	-86.8	0.167	1.471
H_2CO	$J_{K_a,K_c} = 3_{2,2} - 2_{2,1}$	2.0	218.475632	0.17×0.13	-86.6	1.34	0.529

generally derived from Class II disks (Kusaka et al. 1970; Chiang & Goldreich 1997; Huang et al. 2018). One likely explanation for this high-brightness temperature is that IRS5N experiences self-heating through accretion luminosity, which has also been seen in other eDisk sources and is further explored in S. Takakuwa et al. (2023, in preparation). The total integrated flux density of IRS5N is 101 mJy, measured by integrating pixels with an intensity above 3σ . The geometrical peak position of IRS5N is $19^{\rm h}01^{\rm m}48^{\rm s}.48$, $-36^{\circ}57'15''$. 39. The full width at half maximum (FWHM) of IRS5N is estimated to be \sim 62 au from the Gaussian fit model of the continuum emission. The deconvolved size enables us to estimate the inclination, i, of the IRS5N disk to be \sim 65°, calculated from $i = \arccos(\theta_{\rm min}/\theta_{\rm maj})$, where $\theta_{\rm min}$ and $\theta_{\rm max}$ are the FWHM of the minor and major axes, respectively.

Figure 1(c) shows the zoomed-in view of the binary source IRS5, and panels (d) and (e) show the zoom-in of IRS5b and IRS5a, respectively. Nisini et al. (2005) first reported a separation of \sim 0." 6 between the two components based on pre-images with a relatively coarse pixel size of 0." 14 pixel⁻¹. The pre-images were taken as part of preparations for

spectroscopic observations using the ISAAC instrument of the Very Large Telescope (VLT). Our current high-resolution ALMA observations reveal that IRS5a and IRS5b have a projected separation of ~ 0.9 (~ 132 au at a distance of 147 pc). This difference between the previous and the new separation may be due to a combination of the proper motions of the sources and the confusion from the scattered light in the infrared observations. The peak position of IRS5a as measured with Gaussian fitting is $19^{h}01^{m}48.030, -36^{\circ}57'23.''06$. We adopt this position as the coordinate of IRS5a. IRS5a is peaked at the center, with a peak intensity of 3.87 mJy beam⁻¹ or \sim 62 K and a flux density of 4.85 mJy. The secondary source, IRS5b, is much smaller and fainter than IRS5a. The peak position of IRS5b as $19^{h}01^{m}48.084$ measured with Gaussian fitting is $-36^{\circ}57'22''$ 46. It has a peak intensity of \sim 0.20 mJy beam⁻¹ or \sim 3 K and a flux density of 0.26 mJy. The flux density of IRS5 was also measured by integrating above the 3σ level over a region surrounding the individual continuum sources. From our observations, IRS5a is marginally resolved, whereas IRS5b is not resolved.

Table 2
Estimated Disk Masses of Continuum Emission Sources

Source	Flux Density	Gas+Dust Mass		
	•	20 K	47 K	
	(mJy)	(M_{\odot})	(M_{\odot})	
IRS5N	100.65	0.019	6.65×10^{-3}	
IRS5a	4.85	8.92×10^{-4}	3.20×10^{-4}	
IRS5b	0.26	4.73×10^{-5}	•••	

3.2. Disk and Envelope Masses

The dust continuum emission with ALMA can be used to estimate the mass of the total disk structure surrounding the sources. When we assume optically thin emission, well-mixed gas and dust, and isothermal dust emission, the dust mass can be derived from

$$M_{\rm dust} = \frac{D^2 F_{\lambda}}{\kappa_{\lambda} B_{\lambda}(T_{\rm dust})},\tag{1}$$

where D is the distance to the source (\sim 147 pc), and $T_{\rm dust}$ is the temperature of the disk. F_{λ} , κ_{λ} , and B_{λ} are the flux density of the disk, the dust opacity, and the Planck function at the wavelength λ , respectively. Typically, for Class II disks, $T_{\rm dust}$ is often taken to be a fixed temperature of 20 K independent of the total luminosity (e.g., Andrews & Williams 2005; Ansdell et al. 2016). However, for younger more embedded Class 0/I disks, Tobin et al. (2020) found through radiative transfer modeling that the dust temperature scales as

$$T_{\rm dust} \approx 43 \text{ K} \left(\frac{L_{\rm bol}}{1L_{\odot}}\right)^{0.25}$$
 (2)

For IRS5N with a bolometric luminosity of 1.40 L_{\odot} , Equation (2) yields $T_{\rm dust} = 47$ K.

We estimate the disk masses using both dust temperatures. We adopt $\kappa_{1.3~\text{mm}} = 2.30~\text{cm}^2~\text{g}^{-1}$ from dust opacity models of Beckwith et al. (1990) and assume a canonical gas-to-dust ratio of 100:1 to calculate the disk masses using Equation (1). The resulting total disk mass for IRS5N is 0.019 M_{\odot} for a dust temperature of 20 K and $6.65 \times 10^{-3}~M_{\odot}$ for a dust temperature of 47 K. The scaled dust temperature of IRS5a is similar to that of IRS5N, as Lindberg et al. (2014) found $L_{\rm bol}$ of IRS5a to be 1.7 L_{\odot} . Disk masses are also derived for the binary, IRS5. The estimated disk masses for all the continuum sources are presented in Table 2. It is important to note that the disk masses calculated using Equation (1) represent lower limits because the continuum emission is most likely optically thick (see Section 4).

For comparison, we estimate the mass of the envelope around IRS5N using a simple 1D dust radiative transfer model. We adopt a single power-law density profile, $n \propto r^{-1.5}$, corresponding to material in freefall between inner and outer radii of 100 and 10,000 au, respectively, and take the bolometric luminosity of the source determined from the full SED as the sole (internal) heating source of the dust. The dust radiative transfer model then calculates the temperature profile of the dust in the envelope self-consistently and predicts the SED of the resulting source emission. To constrain the envelope mass, we then fit the long wavelength ($\lambda > 60 \ \mu m$) part of the SED of IRS5N. This method allows for a slightly more robust way of determining the envelope mass than simply

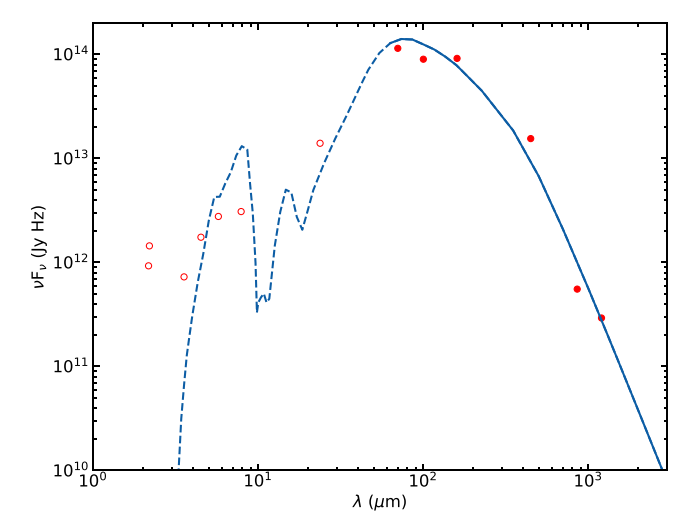


Figure 2. Fitting of the SED of IRS5N with a 1D radiative transfer model. The filled red circles represent SED values over $60 \mu m$ that are fit by the model. The open red circles represent the remaining SED values we used as input. The solid blue line represents the fit given by the model. The dashed blue line shows that the model does not fit this part of the SED.

adopting a single submilimeter flux point and isothermal dust as it provides an estimate of the temperature of the dust that takes the source luminosity into account (e.g., Jørgensen et al. 2002; Kristensen et al. 2012). The resulting fit of the envelope model is shown in Figure 2, with the envelope mass constrained to be $1.2\,M_\odot$. The estimated uncertainty on the fitted envelope mass is comparable to the flux calibration uncertainty, typically about 20% for the measurements used here. However, systematic uncertainties of the adopted simplified physical structure of the envelope and the dust opacity laws will likely dominate this. It is worth emphasizing that this simplified model is not expected to and does not fit the emission at wavelengths shorter than 60 μ m due to the complex geometry of the system at small scales and contributions from scattering.

3.3. Molecular Lines

Of the molecules mentioned in Section 2, emission is detected in $C^{18}O$, ^{12}CO , ^{13}CO , and H_2CO molecules in our observations. Figure 3 presents an overview of the integrated-intensity (moment-0) and mean-velocity (moment-1) maps of all the detected molecules toward IRS5N and IRS5. The moment-1 maps were generated by integrating the regions where $I_{\nu} \geqslant 3\sigma$, where σ is the rms per channel. The maps for $C^{18}O$ and $C^{12}O$ were made using a robust parameter of 0.5, while the maps for the remaining molecules were made using a robust parameter of 2.0. The channel maps of all the observed molecules around IRS5N are shown in the Appendix.

It is worth emphasizing that large-scale negative components are visible in the channel maps of the molecules, particularly of the CO isotopologs. These negative components indicate that a significant amount of extended flux originating from the large-scale structures surrounding the sources is being resolved out. While it is crucial to analyze these structures to build a comprehensive picture of the physics and chemistry of the system, we are constrained by the limitations of our high-resolution observations. The maximum recoverable scale, (θ_{MRS}) , of our observations was 2."91. Hence, this study

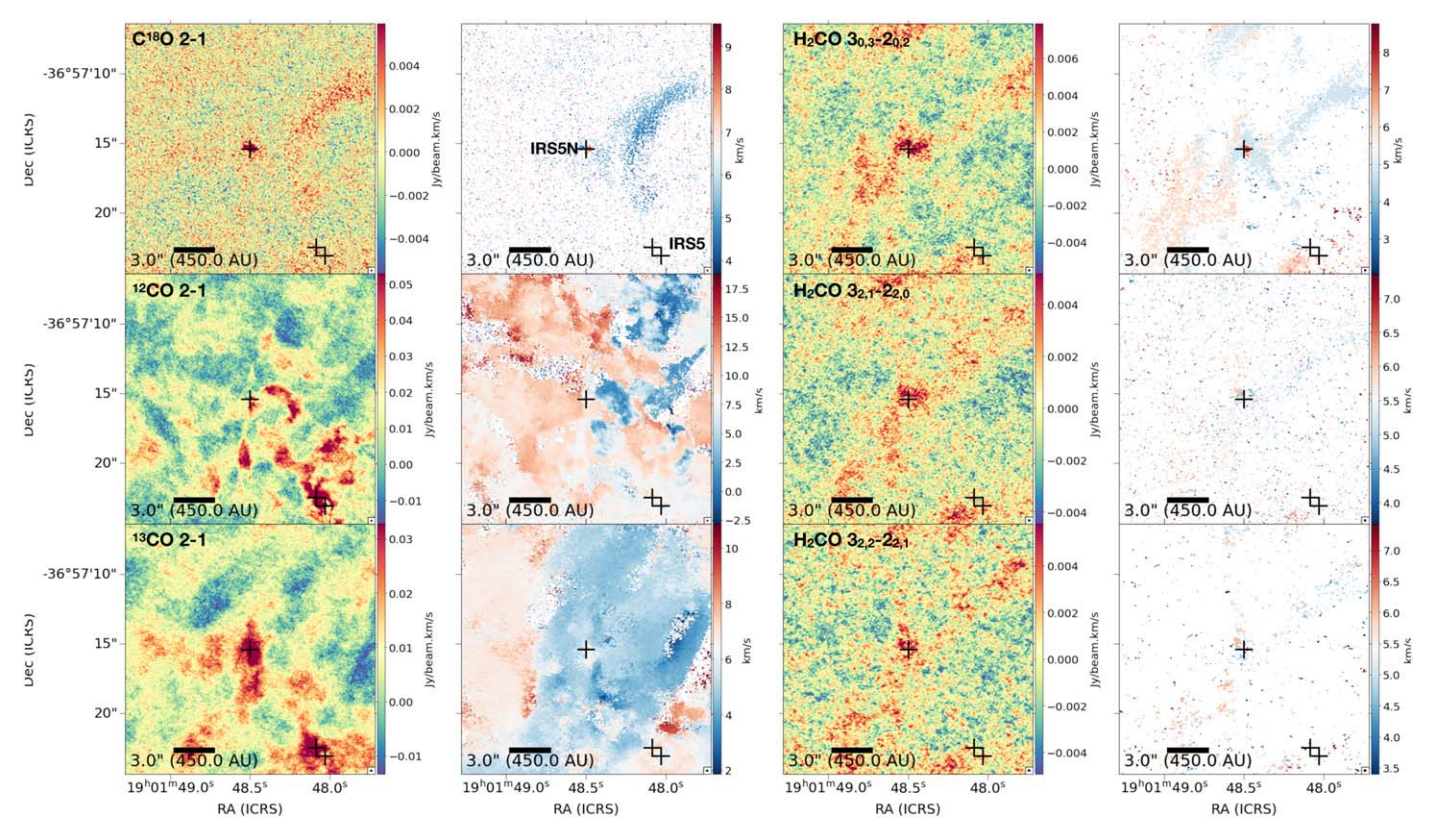


Figure 3. Overview of all the molecular lines detected toward IRS5N and IRS5. For each molecule, the moment-0 map is shown on the left and the moment-1 map is shown on the right. The cross marks show the peak of the continuum emission of IRS5N and the binary IRS5. The maps are created by integrating over the velocity ranges of $3.68-9.53~\rm km~s^{-1}$, $-5.38-20.65~\rm km~s^{-1}$, $0.51-12.03~\rm km~s^{-1}$, $2.06-8.76~\rm km~s^{-1}$, $3.68-7.36~\rm km~s^{-1}$, and $3.40-7.42~\rm km~s^{-1}$ for $C^{18}O$, ^{12}CO , ^{13}CO , ^{12}CO , ^{13}CO , ^{12}CO , ^{13}CO , ^{12}CO , ^{13}CO , $^{$

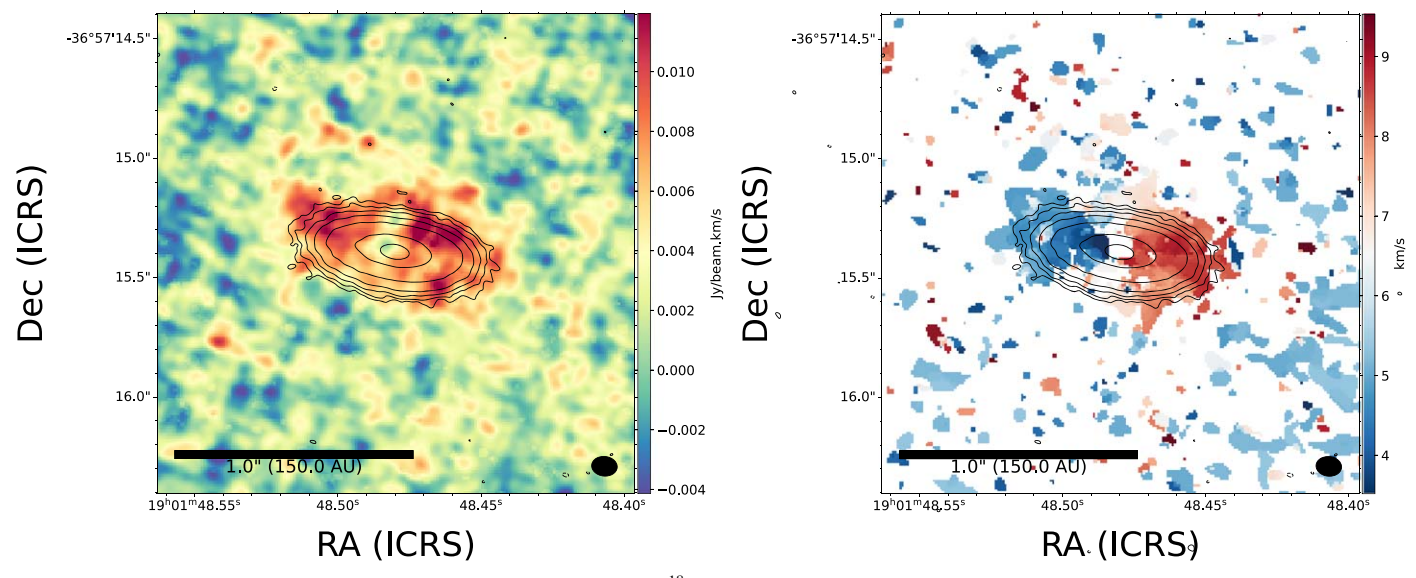


Figure 4. Zoomed-in moment-0 map (*left*) and moment-1 map (*right*) of the $C^{18}O$ (J=2-1) emission toward IRS5N created with the robust value of 0.5. The overlaid contours show continuum emission from 3σ to 192σ , and each contour doubles the previous σ level. The maps are created by integrating over the velocity ranges of 3.68-9.53 km s⁻¹. The synthesized beam size for the $C^{18}O$ emission is $0\rlap.''11 \times 0\rlap.''$ 08.

focuses only on small-scale structures, such as the disk and envelope of individual systems.

3.3.1. $C^{18}O$

Figure 4 shows the zoomed-in integrated moment-0 and moment-1 maps of the C¹⁸O (2-1) emission around IRS5N.

The moment-0 map shows a flattened structure along with a velocity gradient extended along the major axis of the disk, traced by the continuum emission. The size of the gas disk radius from the $\rm C^{18}O$ emission is comparable to that of the disk continuum and has a hole at the protostar position. Based on the consistency between the $\rm C^{18}O$ emission and the continuum emission, the radius of the disk can be assumed to be the same

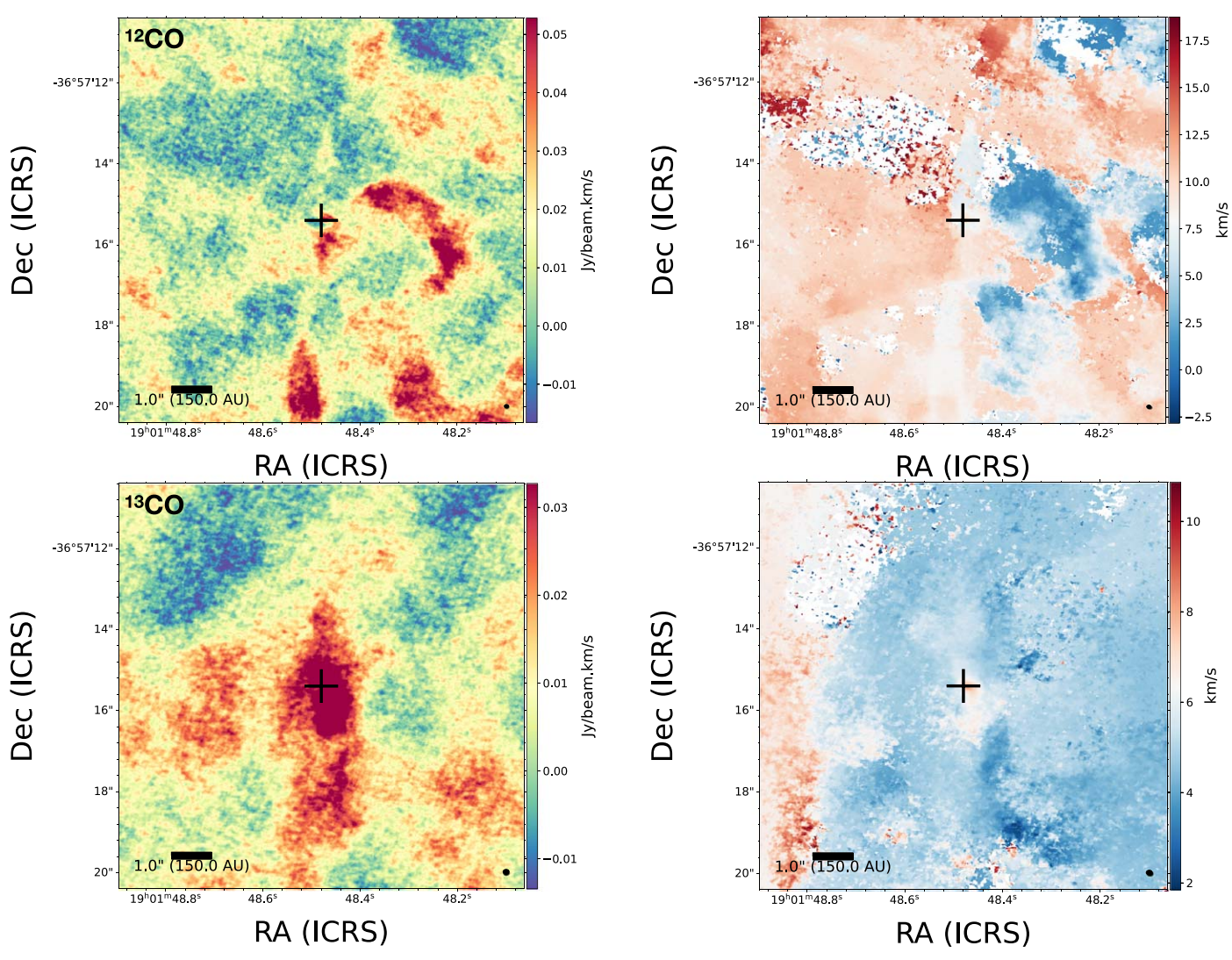


Figure 5. Zoomed-in moment-0 (*left*) and moment-1 (*right*) maps of 12 CO (*top*) and 13 CO (*bottom*) emission. The maps are created by integrating over the velocity ranges of -5.38 to 20.65 km s⁻¹ and 0.51–12.03 km s⁻¹ for 12 CO and 13 CO, respectively. The cross represents the peak position of the IRS5N continuum. The synthesized beam is shown in black in the bottom right corner of each image.

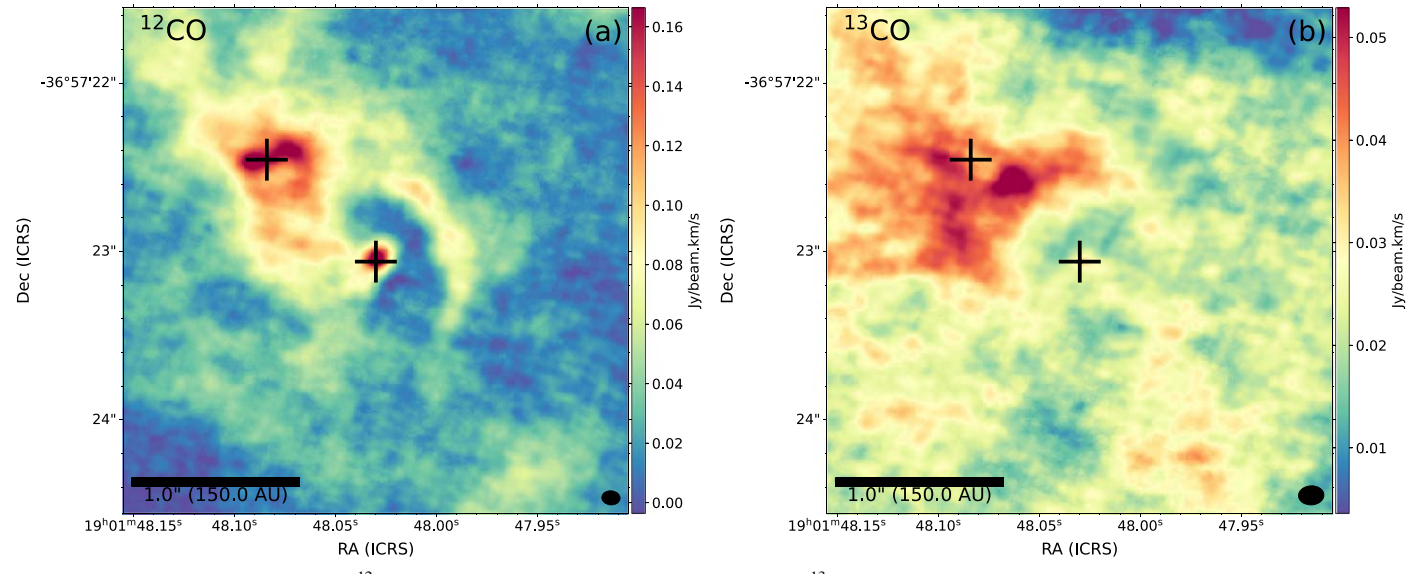


Figure 6. Zoomed-in moment-0 maps of 12 CO emission (a) around the IRS5 binary source and 13 CO emission (b) around the IRS5 binary source. The crosses represent the peak position of the continuum emission of IRS5a and IRS5b sources. The maps are created by integrating over the velocity ranges of -4.75–14.93 km s⁻¹ and 2.85–9.86 km s⁻¹ for 12 CO and 13 CO, respectively. The synthesized beam is shown in black in the bottom right corner of each image.

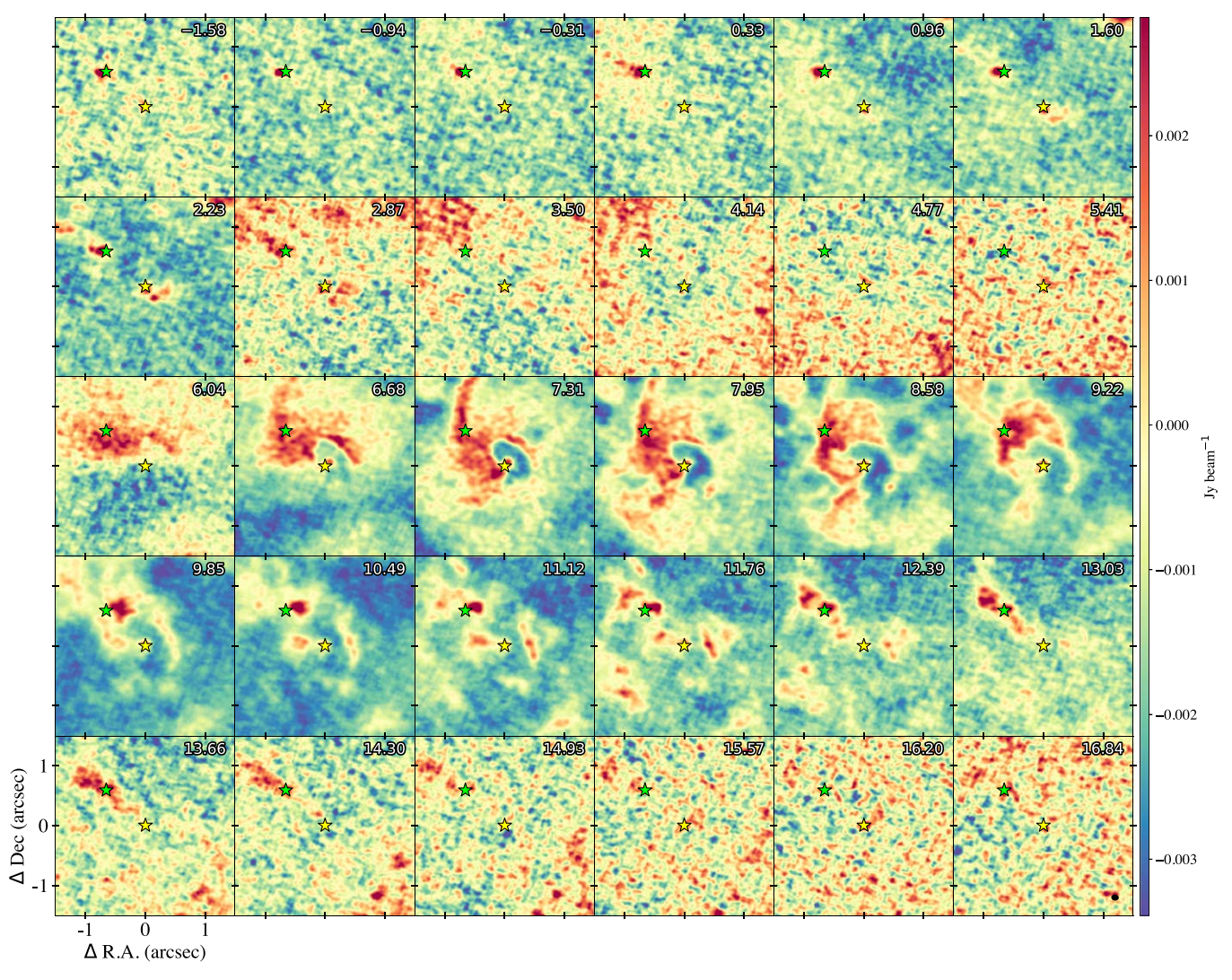


Figure 7. Channel maps showing the ¹²CO emission around the two sources of the IRS5 system. The yellow and green stars show the peak position of the continuum emission of IRS5a and IRS5b, respectively. The numbers at the top show the corresponding velocity of each channel map. The synthesized beam is shown in black in the bottom right corner of the final channel map.

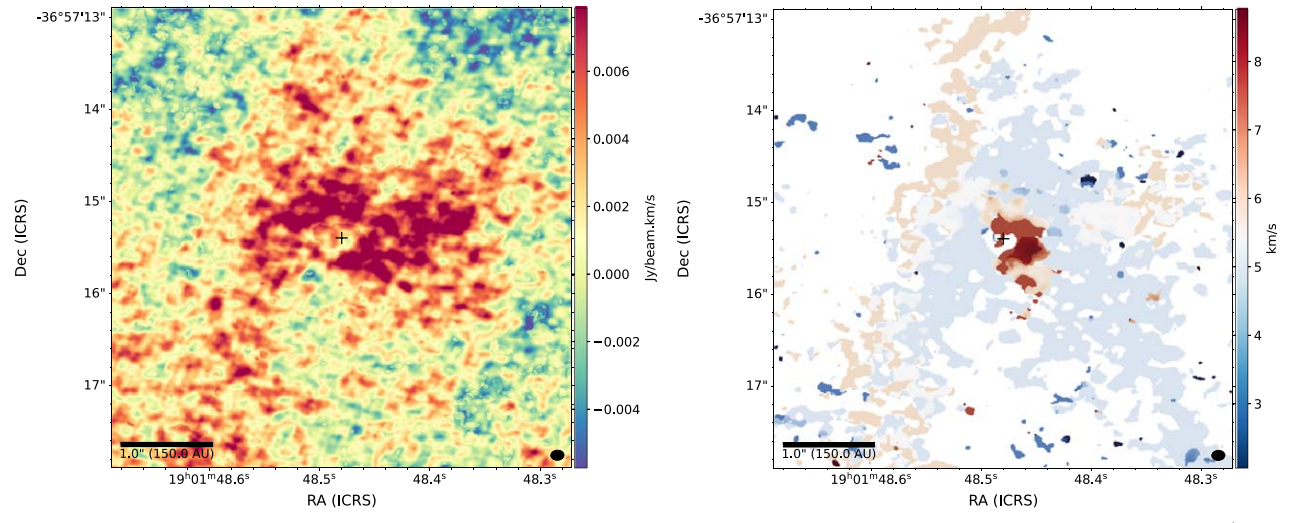


Figure 8. Same as Figure 5, but for H_2CO (3_{0,3}-2_{0,2}). The maps are created by integrating over the velocity ranges of 2.06–8.76 km s⁻¹.

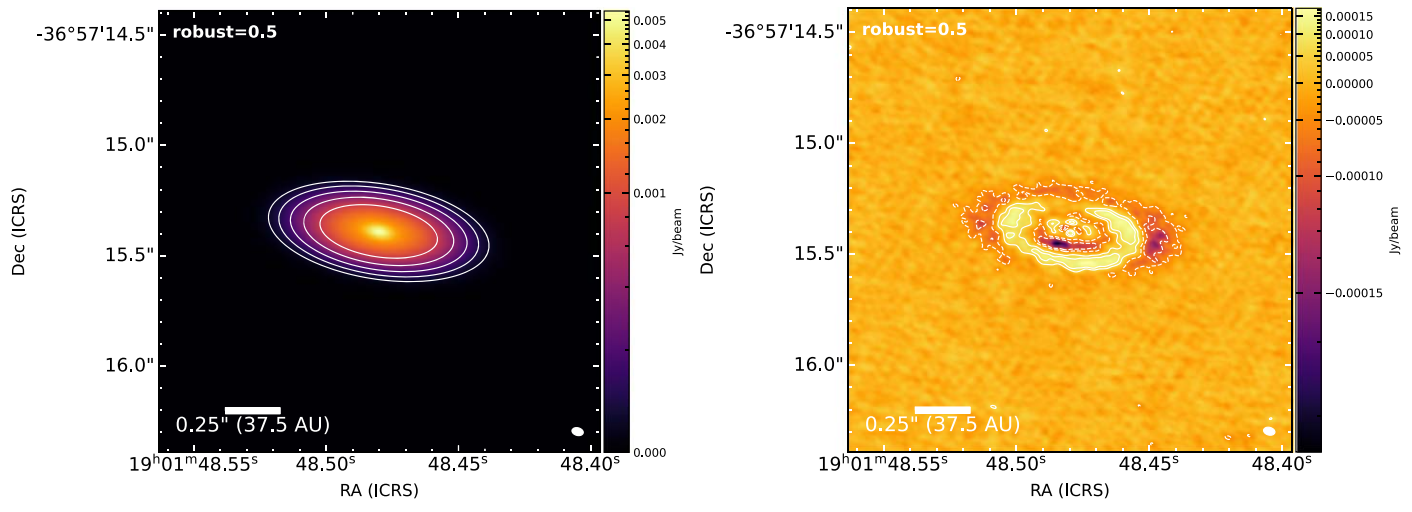


Figure 9. IRS5N disk model (*left*) and residual (*right*) created using double-Gaussian components. The contours show the 3σ , 6σ , 12σ , 24σ , and 48σ . The dashed contours indicate negative intensity. The white ellipse in the bottom right corner of each image shows the synthesized beam.

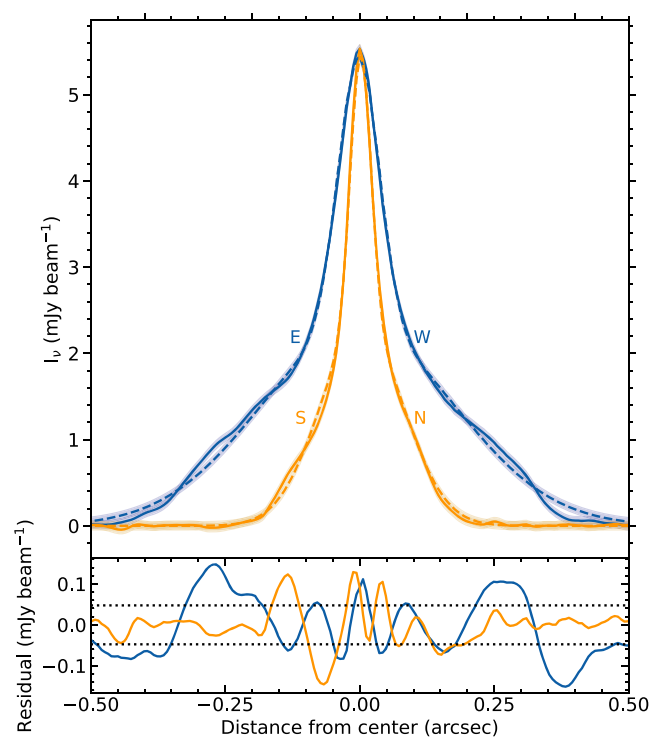


Figure 10. Intensity profiles of the 1.3 mm continuum emission of IRS5N shown in Figure 1(b) and the double-Gaussian component model shown in Figure 9. The solid line represents the observed emission, and the dashed line represents the model. The blue lines indicate the intensity along the major axes, and the orange lines represent the intensity along the minor axes. The smaller plot at the bottom shows the residual intensity after subtracting the model from the observation. The shaded region and the horizontal dotted lines indicate $\pm 3\sigma$ uncertainties with $\sigma = 0.016$ mJy beam $^{-1}$.

as the FWHM of the continuum, \sim 62 au. The hole at the protostellar position has negative intensities below 3σ at 5.35–6.02 km s⁻¹ (see Figures A1, A7). The deficit likely results from continuum oversubtraction that is caused by the relatively weak C¹⁸O emission compared to the bright continuum emission.

The moment-1 map of the C¹⁸O emission shows that the blue- and redshifted velocities have a distinct separation along the eastern and western sides, respectively. This velocity profile

is consistent with a rotating disk. The position–velocity (PV) analysis of the C¹⁸O emission is presented in Section 4.

3.3.2. ¹²CO and ¹³CO

Figure 5 shows zoomed-in moment-0 and moment-1 maps of 12 CO (2–1) and 13 CO (2–1) emission near IRS5N. While the ¹²CO emission shows extended emission around IRS5N, it does not seem to trace any obvious outflow/jet associated with the protostar, which is puzzling. The spiral structure seen west of the protostar is blueshifted and seems to trace infalling material onto the protostellar disk (see the channel maps; Figure A2). Additionally, extended emission is seen in the surrounding of IRS5N, some of which likely originates from the protostar. In contrast, the ¹³CO plot shows some emission in the north-south direction of the protostar, but this emission is mostly observed in redshifted velocity channels (Figure A9). The channel maps of ¹³CO also show an apparent deficit near the protostellar position at the velocity range of 5.02–6.19 km s⁻¹ that is much more prominent than the deficit seen on the C¹⁸O channel maps (Figure A7). This is most likely due to the continuum oversubtraction, similar to that of the C¹⁸O emission. This suggests that the ¹³CO emission is extended and somewhat optically thick, leading it to become resolved out as $\theta_{\rm MRS} = 2.^{\prime\prime}91$. The moment maps of $^{12}{\rm CO}$ and $^{13}{\rm CO}$ reveal the complex nature of the emission around IRS5N.

We also detected molecular emission in $^{12}\text{CO}(2-1)$ and $^{13}\text{CO}(2-1)$ toward IRS5. Figure 6(a) shows the moment-0 maps of ^{12}CO emission around IRS5a and IRS5b. The ^{12}CO emission around IRS5a is compact, without visible outflow structure. In contrast, bright elongated emission is observed toward IRS5b in the east—west direction, possibly tracing an outflow from IRS5b. The emission has a velocity gradient and relatively high velocities from -1.58 to 2.23 km s⁻¹ and 9.85 to 13.03 km s⁻¹, as shown in the ^{12}CO channel maps in Figure 7. Additionally, bright extended emission is also seen around IRS5b, which connects its way into IRS5a. Based on the ^{12}CO emission toward the IRS5 binary, we estimate its systemic velocity to be \sim 6.50 km s⁻¹. The channel maps show that the blueshifted emission seems to emanate from IRS5b and stream onto IRS5a as the velocity increases. Similar stream- or bridge-like features are observed toward other protostellar binaries (e.g., Sadavoy et al. 2018; van der Wiel et al. 2019; Jørgensen et al.

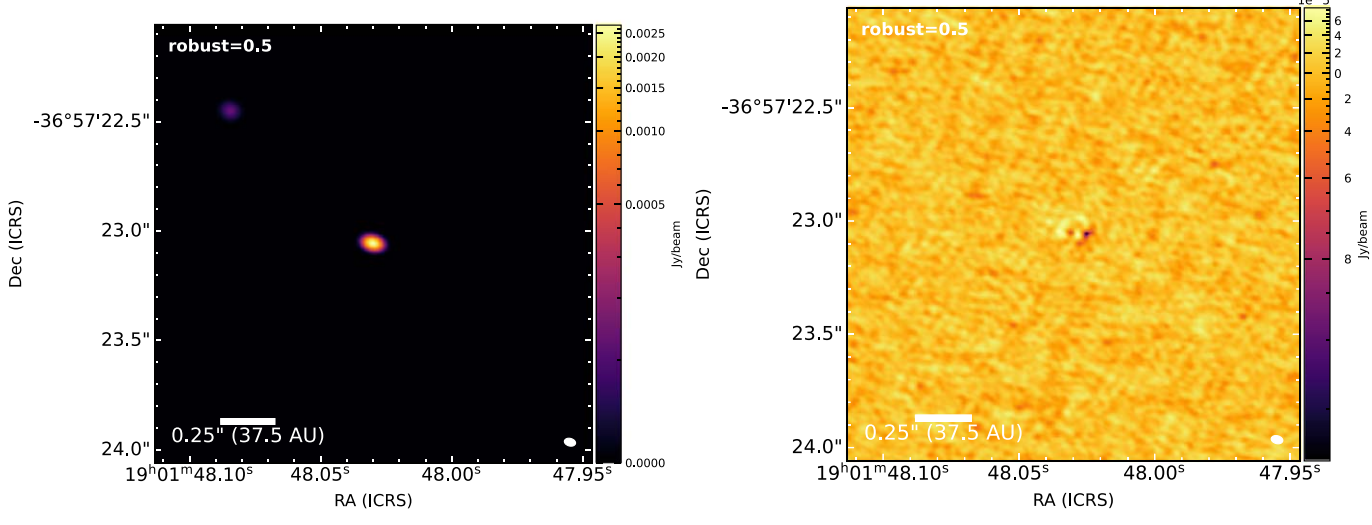


Figure 11. Same as Figure 10, but for tje IRS5a binary source with the model made with a single-Gaussian peak for each continuum emission observed.

Ta	ble	3
Rest_fit	Para	meters

Parameter	Single-Gaussian Component			Double-Gaussian Components		
	IRS5N	IRS5a	IRS5b	IRS5N		
				Component 1	Component 2	
R.A. (h:m:s)	19:01:48.480	19:01:48.030	19:01:48.084	19:01:48.480	19:01:48.480	
Decl. (d:m:s)	-36:57:15.39	-36:57:23.06	-36:57:22.46	-36:57:15.39	-36:57:15.39	
Beam size (")	0.05×0.03	0.05×0.03	0.05×0.03	0.05×0.03	0.05×0.03	
Beam P.A. (°)	75.44	75.44	75.44	75.44	75.44	
$\theta_{\rm mai} \ ({\rm mas})^{\rm a}$	373.7 ± 7.1	22.91 ± 0.95	46 ± 16	73.58 ± 1.69	423.9 ± 3.0	
θ_{\min} (mas) ^a	156.7 ± 2.9	16.82 ± 0.56	40 ± 26	28.32 ± 0.76	179.4 ± 1.3	
P.A. (°) ^a	81.10 ± 0.76	84.7 ± 5.7	174 ± 54	81.22 ± 0.80	81.08 ± 0.29	
Inclination (°)	65.21 ± 0.70	42.76 ± 3.29	29.59 ± 74.38	67.36 ± 0.84	64.96 ± 0.27	
Peak intensity (mJy beam ⁻¹)	2.970 ± 0.054	3.893 ± 0.020	0.174 ± 0.00022	3.172 ± 0.039	2.286 ± 0.016	
Flux density (mJy)	99.1 ± 1.9	4.727 ± 0.041	0.361 ± 0.00063	7.09 ± 0.12	98.30 ± 0.69	

Note.

2022) and may trace transport of material between the companions triggered by interactions during their mutual orbits (e.g., Kuffmeier et al. 2019; Jørgensen et al. 2022). The streaming emission appears to end in a disk-like structure around IRS5a, seen in channel maps of 6.68–9.85 km s⁻¹. Notably, this structure is much larger than the observed size of the dust continuum structure of IRS5a seen in Figure 1, indicating it likely traces the inner envelope surrounding the disk. Additionally, in channel maps ranging from 7.31 to 8.58 km s⁻¹, extended emission possibly tracing an outflow is seen toward the southeast of IRS5a. Conversely, the ¹³CO emission in Figure 6(b) traces the extended mutual envelope material surrounding both sources. The emission is much brighter toward IRS5b than IRS5a, with the brightness peak toward the southwest of IRS5b.

3.3.3. H₂CO

In addition to the CO isotopologs, we also detect emission from three H₂CO lines toward IRS5N. Figure 3 shows that the emission structures of the three transitions are similar to one another, with most of the emission surrounding the disk and inner envelope, with extended emission toward the northwest and southeast direction of the source. There is a slight velocity

Table 4PV Fitting Results for C¹⁸O with SLAM

Fitting Method	Edge	Ridge	
R _b (au)	76.98 ± 2.30	42.80 ± 0.44	
p_{in}	0.554 ± 0.047	0.379 ± 0.012	
$v_{\rm sys}~({\rm km~s}^{-1})$	6.564 ± 0.024	6.507 ± 0.008	
$M_{\rm in}~(M_{\odot})$	0.398 ± 0.041	0.184 ± 0.008	

difference between the two sides of the extended source, as shown by the moment-1 maps. The $3_{0,3}$ – $2_{0,2}$ transition has the lowest upper-level energy and is also the strongest, as expected. A magnified view of the moment-0 and moment-1 maps of the brightest transition of H_2CO , $3_{0,3}$ – $2_{0,2}$, is shown in Figure 8. The zoomed-in maps reveal that in addition the large-scale emission, some redshifted emission is visible toward the west of the disk, similar to that of the $C^{18}O$ emission (see Figure 4), but it appears to lack the corresponding blueshifted counterpart, suggesting asymmetric distribution of the chemical composition of the disk/envelope system. The velocity channel maps show that there is negative emission at the position of the protostar that again is likely caused by continuum

^a Values are deconvolved from the beam.

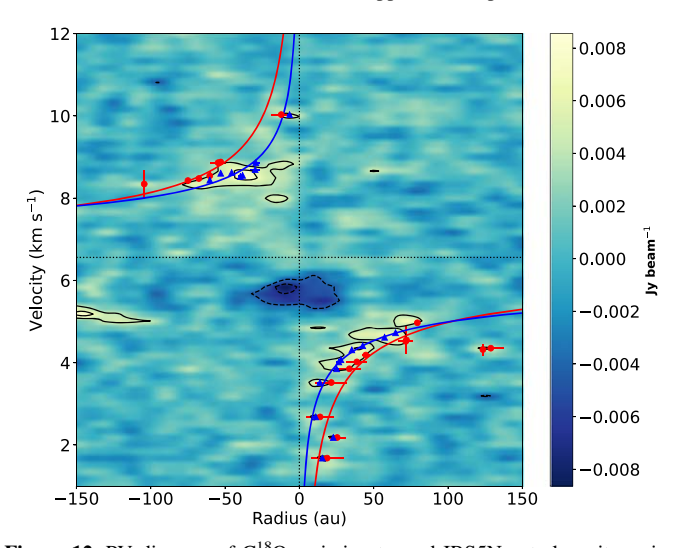


Figure 12. PV diagram of $C^{18}O$ emission toward IRS5N cut along its major axis. The points derived using the edge and ridge methods and their corresponding rotation curves are shown in blue and red, respectively. The black contours start at the 3σ level and increase every 2σ . The dashed contours show the corresponding negative contours.

oversubtraction (see Figures A4, A10). However, the largescale negatives seen in the velocity channel maps suggest that a significant amount of flux is resolved out.

4. Analysis and Discussion

4.1. Continuum Modeling

As shown in Figure 1, even though we sufficiently resolve the disk of IRS5N, no apparent substructures can be identified in the continuum emission. IRS5a also appears to be relatively smooth, while IRS5b is not resolved.

Figure 9 shows the best-fit model and its corresponding residual of the continuum emission of IRS5N made with the CASA task imfit. The model was created using two 2D Gaussian components as a single-Gaussian model misses much of the emission of the continuum. The residual image and the intensity plots in Figure 10 show that the double-component model is able to recover most of the continuum emission. The fitting results of both models are provided in Table 3. The parameters of the disk continuum such as its peak position, P.A., and i do not change significantly between the two components of the model. It is important to note that the residuals arise because the model does not represent the structure of the emission, and they cannot necessarily be taken as evidence of the presence of substructures in the distribution of material within the dusty disk. The residual image shows that there is some asymmetry in the direction of the minor axis (north-south). The disk appears to be brighter in the south compared to the north. This asymmetry in the minor axis is observed in several eDisk sources (Ohashi et al. 2023). This can be attributed to the geometrical effects of optically thick emission and flaring of the disk (S. Takakuwa et al. 2023, in preparation). The north side of the disk is more obscured compared to the south, which is expected to be on the far side of the disk with $i \sim 65^{\circ}$, where 90° represents the completely edge-on case.

We also fit the continuum emission for both sources in the IRS5 system. Figure 11 shows the model and the residual created of IRS5a and IRS5b after subtracting a single 2D

Gaussian. The model is able to reasonably capture the majority of the continuum emission from both sources, as seen from the residual images. The results of the fitting are provided in Table 3.

4.2. Kinematics of the Disk: Position-Velocity Diagram

The kinematics of the protostellar disk are investigated with PV diagrams of molecular line emission that trace the disk. For IRS5N, C¹⁸O is the only molecule where evidence of rotation is seen in the protostellar disk (see Figure 3). C¹⁸O is much less optically thick and is a better disk tracer than other CO isotopologs, making it an excellent species for a PV analysis. Figure 12 shows the PV diagram of IRS5N in C¹⁸O along the major axis of the disk. The PV diagram shows that the blue-and redshifted emission are separated in the northeast and southwest, respectively.

The PV diagram was fit using the pvanalysis package of the spectral line analysis/modeling (SLAM)¹⁹ code (Aso & Sai 2023) to investigate the nature of the rotation. The details of the fitting procedure are given in Ohashi et al. (2023), but a short description is provided here. The code determines the corresponding position at a given velocity using the PV diagram and calculates two types of representative points known as the edge and the ridge. The ridge is defined as the intensity-weighted mean calculated with emission detected above a given threshold, while the edge corresponds to the outermost contour defined by a given threshold. For the analysis of the PV diagram of the $C^{18}O$ emission around IRS5N, a threshold of 3σ level was used, where $\sigma=1.636$ mJy beam⁻¹. The edge and the ridge are then fit separately with a single power-law function given by

$$V_{\rm rot} = V_b \left(\frac{R}{R_b}\right)^{-p} + V_{\rm sys},\tag{3}$$

where V_{rot} is the rotational velocity, R_b is the break radius, V_b is the rotational velocity at R_b , p is the power-law index, and V_{sys} is the systemic velocity of the system.

The fitting results of the SLAM code are summarized in Table 4. Here, the ridge points are calculated using the 1D intensity-weighted mean profile, called "mean" fitting method. However, the ridge points can also be calculated using the center of the Gaussian fitting. Using this Gaussian fitting method, we obtain $R_{\rm b} = 39.75 \pm 0.76$ au, $p_{\rm in} = 0.515 \pm 0.029$, $v_{\rm sys} = 6.464 \pm 0.020$ km s⁻¹, and $M_{\rm in} = 0.246 \pm 0.015$ (M_{\odot}), which are consistent with the values derived from the mean method. In the case of both the edge and ridge methods, the value of $p_{\rm in}$ is found to be close to 0.5, suggesting that the disk of IRS5N is already in Keplerian rotation. Typically, Keplerian rotation is commonly observed in more evolved sources (Simon et al. 2000). However, recent studies have found that some Class 0 sources already possess Keplerian disks (e.g., Tobin et al. 2012; Ohashi et al. 2014, 2023). In both the ridge and the edge methods, Keplerian rotation is observed out to a radius of \sim 40 au and \sim 76 au, respectively. The FWHM of the disk continuum falls well within this range, indicating that it could serve as a reliable indicator of the disk size of IRS5N. Under this assumption, the mass of the central source of IRS5N is estimated to be $0.398 \pm 0.041~M_{\odot}$ and $0.184 \pm 0.008~M_{\odot}$ for the edge and the ridge cases, respectively. The actual mass of

¹⁹ https://github.com/jinshisai/SLAM

the central source likely lies between these two estimates, approximately $0.3\,M_\odot$ (Maret et al. 2020). This shows that with a stellar mass of $\sim\!0.3\,M_\odot$ compared to a disk mass of $\sim\!0.007$ – $0.02M_\odot$ and an envelope mass of $1.2\,M_\odot$, IRS5N is a deeply embedded protostar.

The stability of the disk against gravitational collapse can be estimated by using Toomre's Q parameter,

$$Q = \frac{c_s \Omega}{\pi G \Sigma},\tag{4}$$

where c_s is the sound speed, $\Omega = GM_*/R^3$ is the differential rotation value of a Keplerian disk at the given radius R, M_* is the mass of the protostar, G is the gravitational constant, and Σ is the surface density. A disk is considered gravitationally stable if Q > 1, while Q < 1 suggests that the disk may be prone to fragmentation. This equation can also be expressed in the form given by Kratter & Lodato (2016) and Tobin et al. (2016) as

$$Q \approx 2 \frac{M_* H}{M_d R},\tag{5}$$

where $H = c_s/\Omega$, M_d is the mass of the disk, and R is the radius of the disk. For IRS5N with $M_* = 0.3~M_\odot$ and R = 62 au, we find $Q \approx 3.5$ and 15 for disk masses of 0.019 M_\odot and $6.65 \times 10^{-3} M_\odot$ at 20 K and 47 K, respectively. This implies that the disk of IRS5N is gravitationally stable.

4.3. The Low Molecular Emission around IRS5N

In Section 3 we mention that although we see extended emission in ^{12}CO and ^{13}CO in the region around IRS5N, we do not see any clear signs of outflow in these molecules. Emission is not detected in SiO (J=5–4) or SO ($J=6_5$ –5₄) either, both of which are known tracers of outflow and shocks (e.g., Schilke & Walmsley 1997; Wakelam et al. 2005; Ohashi et al. 2014; Sakai et al. 2014). This is in contrast to most known young Class 0/I sources, where observations of a prominent outflow have become ubiquitous. Additionally, most of the emission detected in H_2 CO, the only other molecule besides the CO isotopologs detected around IRS5N, is at a tentative level of $3\sigma-5\sigma$.

The curious case of low emission around IRS5N has also been noted by previous studies (Nutter et al. 2005; Lindberg et al. 2014). Lindberg et al. (2014) specifically noted that only marginal residuals remained in the Herschel/PACS maps of the region when assuming that all emission originated from the IRS5 source. Recent studies suggest that objects previously thought to be young Class 0 that exhibit weak molecular line emission and lack prominent high-velocity outflow structures may actually be potential candidates for the first hydrostatic core (FHSC; Busch et al. 2020; Maureira et al. 2020; Dutta et al. 2022). These FHSC objects, however, have a relatively short lifetime of ${\sim}10^3$ yr, and simulations predict their luminosities to be ${\sim}0.1~L_{\odot}$ and the mass of their central source to be $\lesssim 0.1~M_{\odot}$ (Commerçon et al. 2012; Tomida et al. 2015; Maureira et al. 2020). Considering that IRS5N has a bolometric luminosity of 1.40 L_{\odot} and a protostellar mass of $0.3 M_{\odot}$, it has already progressed well beyond the FHSC stage, and this most likely is not the explanation for the observed low emission and lack of outflow. Nonetheless, given the presence of a massive envelope of $\sim 1.2 M_{\odot}$ surrounding IRS5N, it is likely to become much more massive in the future.

The peculiarity of the molecular emission characteristics of IRS5N are most likely explained by the complexity of the Coronet region. IRS7B, another YSO source of eDisk from the Coronet region, also seems to lack an outflow in the spectral lines (Ohashi et al. 2023). The Coronet hosts numerous YSOs and molecular hydrogen emission-line objects (MHOs) with more than 20 Herbig-Haro (HH) objects (see Wang et al. 2004, and references therein). This environment might be affecting the molecular emission seen from these sources. ¹²CO, being optically thick, is the most affected. We do observe ¹³CO emission in the north-south direction of the source, roughly in the direction where the outflow is expected. However, this is only seen in low-velocity redshifted channel maps. C18O appears to be the least affected of the CO isotopologs as it is the most optically thin of the three and is not as hidden behind the optically thick emission from the cloud like ¹²CO and ¹³CO, making it mostly sensitive to the inner disk, where the CO is evaporated from the dust grains (Jørgensen et al. 2015).

5. Conclusions

We have presented high-resolution high-sensitivity observations of the protostar IRS5N and its surroundings as part of the eDisk ALMA Large program. Our ALMA Band 6 observation had a continuum angular resolution of $\sim\!0.^{\prime\prime}05~(\sim\!8$ au) and molecular line emission from C¹⁸O, ¹²CO, ¹³CO, and H₂CO. The main results of the paper are as follows:

- 1. The 1.3 mm dust continuum emission traces protostellar disks around IRS5N and IRS5. The continuum emissions appear smooth, with no apparent substructures in either source. However, the disk of IRS5N shows brightness asymmetry in the minor axis, with the southern region appearing brighter than the northern region. The asymmetry can be attributed to the geometrical effects of optically thick emission and flaring of the disk.
- 2. IRS5N has a disk radius of \sim 62 au elongated along the northeast to southwest direction, with a P.A. of 81°.10. IRS5a has a much smaller disk radius of \sim 13 au, with a P.A. of \sim 85°. The disk of IRS5b remains unresolved. Based on the total integrated intensity of each source and assuming a temperature of T=20 K, which is a typical dust temperature for Class II disks, the estimated disk masses for IRS5N, IRS5a, and IRS5b are 0.02, 9.18×10^{-4} , and 6.48×10^{-5} M_{\odot} , respectively. At a temperature of T=47 K based on radiative transfer, the estimated disk masses for IRS5N and IRS5a are 6.65×10^{-3} and 3.20×10^{-4} M_{\odot} , respectively.
- 3. Disk rotation is observed in the $C^{18}O$ emission around IRS5N, with the blue- and redshifted emission separated along the major axis of the disk. The PV analysis of the emission reveals that the disk is in Keplerian rotation. The stellar mass of the central source of IRS5N is estimated to be $\sim 0.3~M_{\odot}$.
- With a 1D dust radiative transfer model, the estimated envelope mass around IRS5N is 1.2 M_☉. The envelope mass is much greater than the disk mass of 0.02 M_☉ and the stellar mass of 0.3 M_☉, indicating that IRS5N is a highly embedded protostar.
 The ¹²CO and ¹³CO maps toward IRS5N are complex
- 5. The ¹²CO and ¹³CO maps toward IRS5N are complex and lack any apparent indication of an outflow or cavity. In contrast, the ¹²CO maps around IRS5 show emission streaming from IRS5b to IRS5a, tracing the gas

connecting to the disk-like structure around the latter. This observation potentially suggests material transport between the two sources.

Acknowledgments

This paper makes use of the following ALMA data: ADS/ JAO.ALMA#2019.1.00261.L. ALMA is a partnership of ESO (representing its member states), NSF (USA), and NINS (Japan), together with NRC (Canada), MOST and ASIAA (Taiwan), and KASI (Republic of Korea), in cooperation with the Republic of Chile. The Joint ALMA Observatory is operated by ESO, AUI/NRAO, and NAOJ. The National Radio Astronomy Observatory is a facility of the National Science Foundation operated under cooperative agreement by Associated Universities, Inc. R.S, J.K.J, and S.G. acknowledge support from the Independent Research Fund Denmark (grant No. 0135-00123B). S.T. is supported by JSPS KAKENHI grant Nos. 21H00048 and 21H04495. This work was supported by NAOJ ALMA Scientific Research Grant Code 2022-20A. L.W.L. acknowledges support from NSF AST-2108794. J.J.T. acknowledges support from NASA XRP 80NSSC 22K1159. N.O. acknowledges support from National Science and Technology Council (NSTC) in Taiwan through grants NSTC 109-2112-M-001-051 and 110-2112-M-001-031. S.P.L. and T.J.T. acknowledge grants from the National Science and Technology Council of Taiwan 106-2119-M-007-021-MY3 and 109-2112-M-007-010-MY3. I.d.G. acknowledges support from grant PID2020-114461GB-I00, funded by MCIN/AEI/ 10.13039/501100011033. Z.Y.D.L. acknowledges support from NASA 80NSSCK1095, the Jefferson Scholars Foundation, the NRAO ALMA Student Observing Support (SOS) SOSPA8-003, the Achievements Rewards for College Scientists (ARCS) Foundation Washington Chapter, the Virginia Space Grant Consortium (VSGC), and UVA research

computing (RIVANNA). Z.-Y.L. is supported in part by NASA NSSC20K0533 and NSF AST-1910106. W.K. was supported by the National Research Foundation of Korea (NRF) grant funded by the Korea government (MSIT; NRF-2021R1F1A1061794). C.W.L. is supported by the Basic Science Research Program through the National Research Foundation of Korea (NRF) funded by the Ministry of Education, Science and Technology (NRF- 2019R1A2C1010851), and by the Korea Astronomy and Space Science Institute grant funded by the Korea government (MSIT; Project No. 2023-1-84000). H.-W.Y. acknowledges support from the National Science and Technology Council (NSTC) in Taiwan through the grant NSTC 110-2628-M-001-003-MY3 and from the Academia Sinica Career Development Award (AS-CDA-111-M03). Y.A. acknowledges support by NAOJ ALMA Scientific Research Grant code 2019-13B, Grant-in-Aid for Transformative Research Areas (A) 20H05844 and 20H05847. J.E.L. is supported by the National Research Foundation of Korea (NRF) grant funded by the Korean government (MSIT; grant No. 2021R1A2C1011718). J.P.W. acknowledges support from NSF AST-2107841.

Facility: ALMA.

Software: CASA (McMullin et al. 2007), Numpy (Harris et al. 2020), Astropy (Astropy Collaboration et al. 2018), Matplotlib (Hunter 2007), APLpy (Robitaille & Bressert 2012; Robitaille 2019), SLAM (https://github.com/jinshisai/SLAM).

Appendix Channel Maps

Figures A1–A6 show the selected large-scale channel maps of ¹²CO, ¹³CO, C¹⁸O, and H₂CO emission observed toward IRS5N. Figures A7–A12 show the zoomed-in view of the molecular emissions observed.

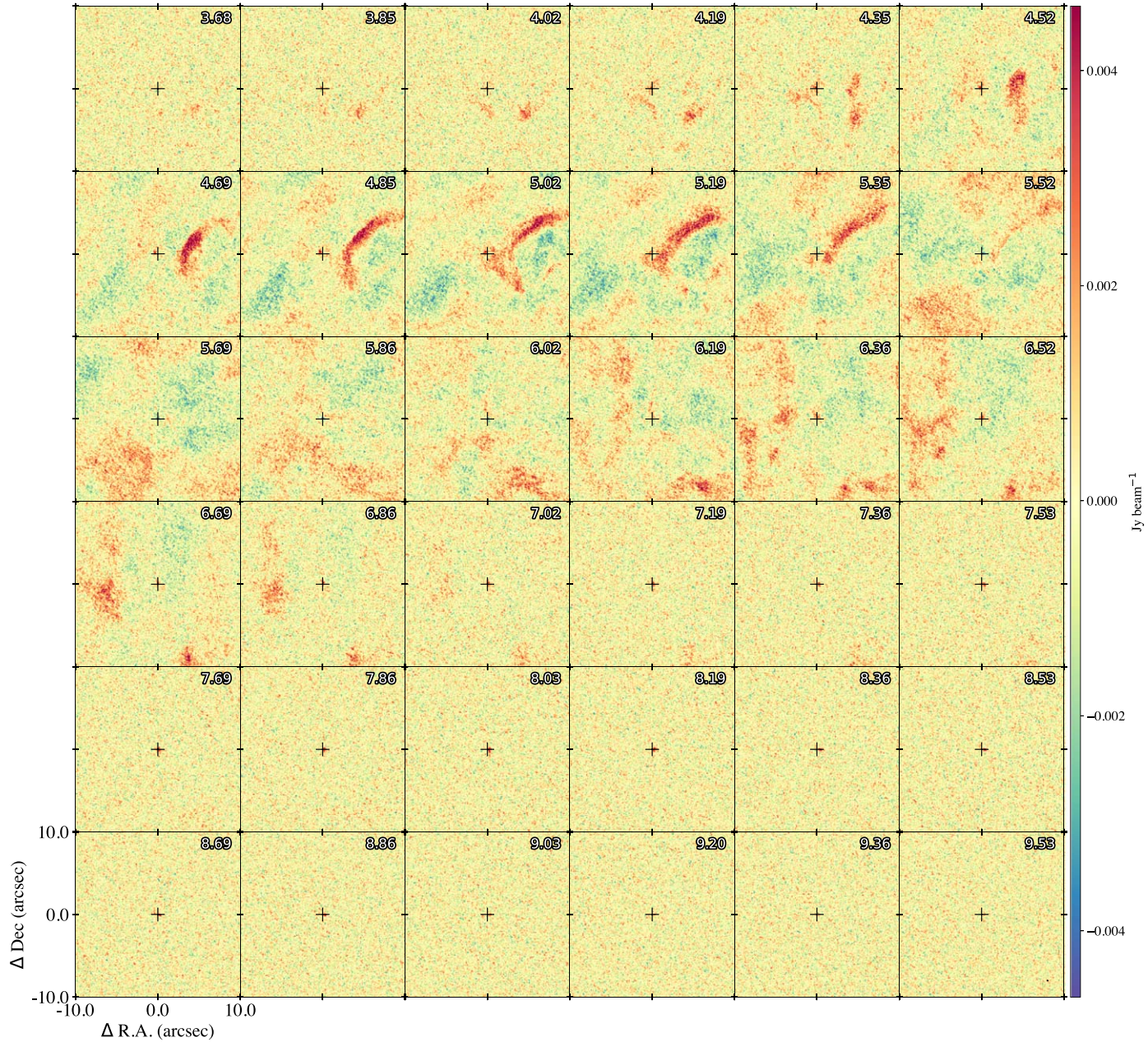


Figure A1. Selected channel maps showing the $C^{18}O(2-1)$ emission around IRS5N. The numbers at the top show the corresponding velocity of each channel map. The cross shows the peak position of the IRS5N continuum. The synthesized beam is shown in black in the bottom right corner of the final channel.

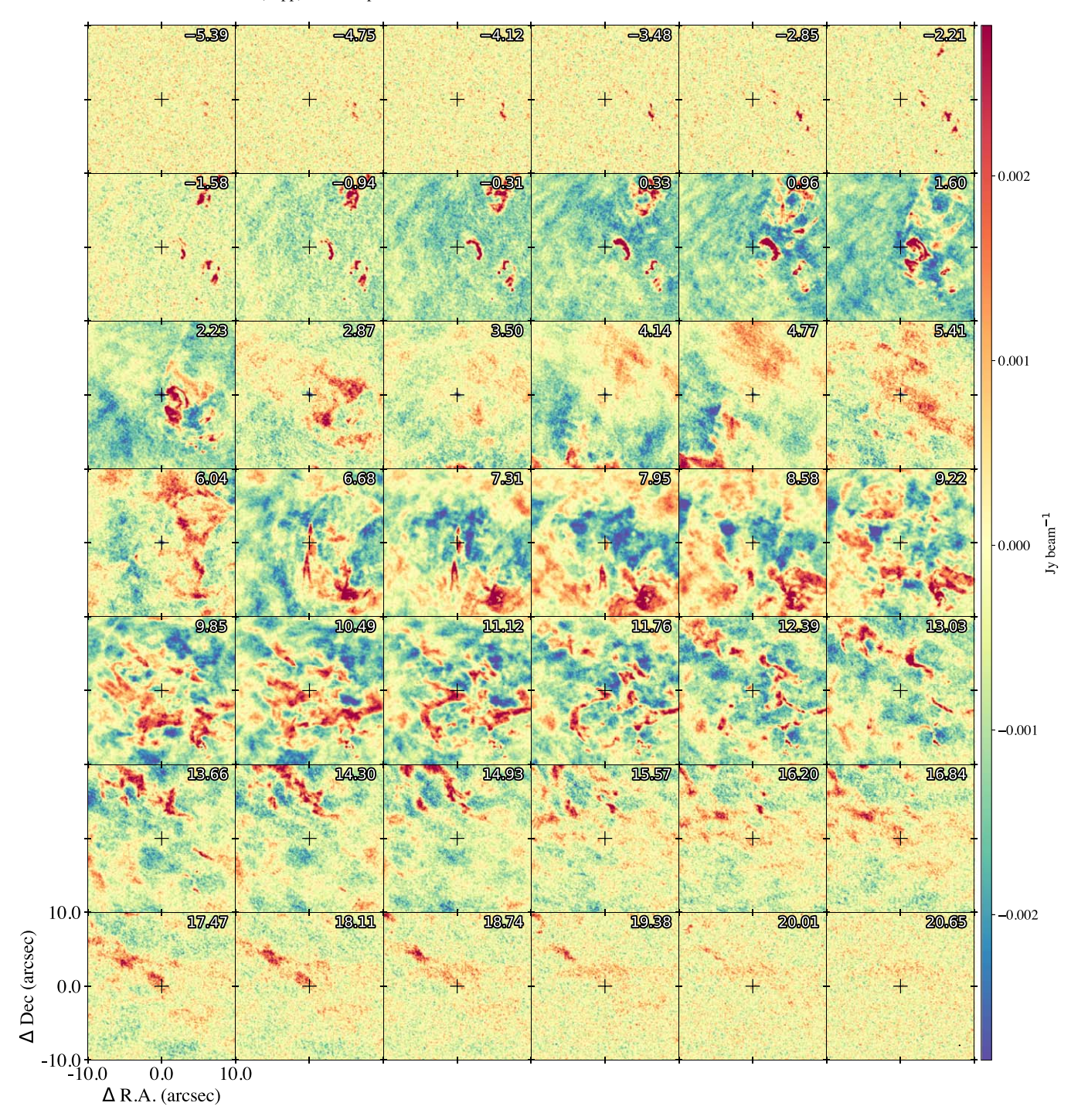


Figure A2. Same as Figure A1, but for $^{12}CO(2-1)$.

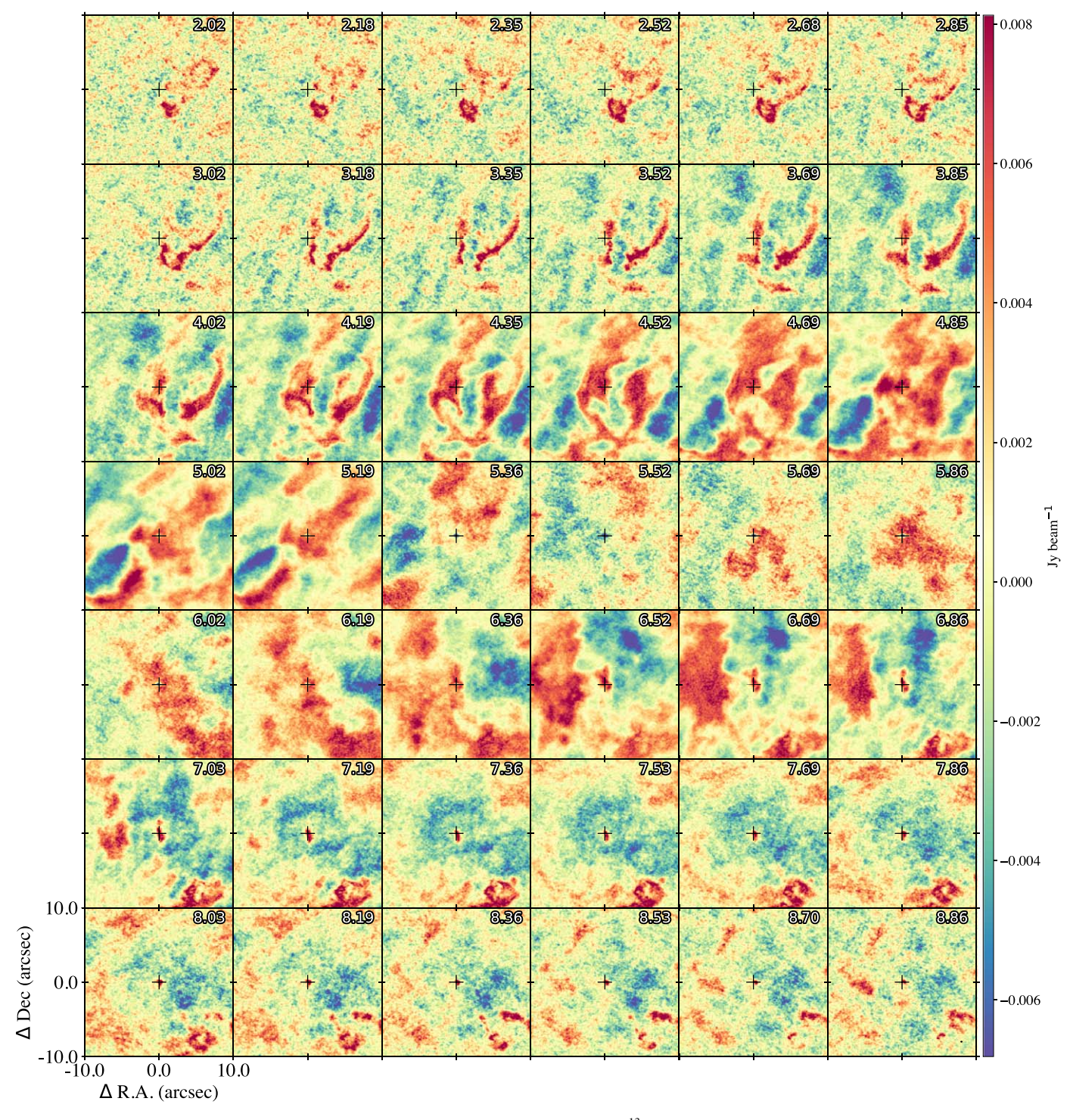


Figure A3. Same as Figure A1, but for ¹³CO (2–1).

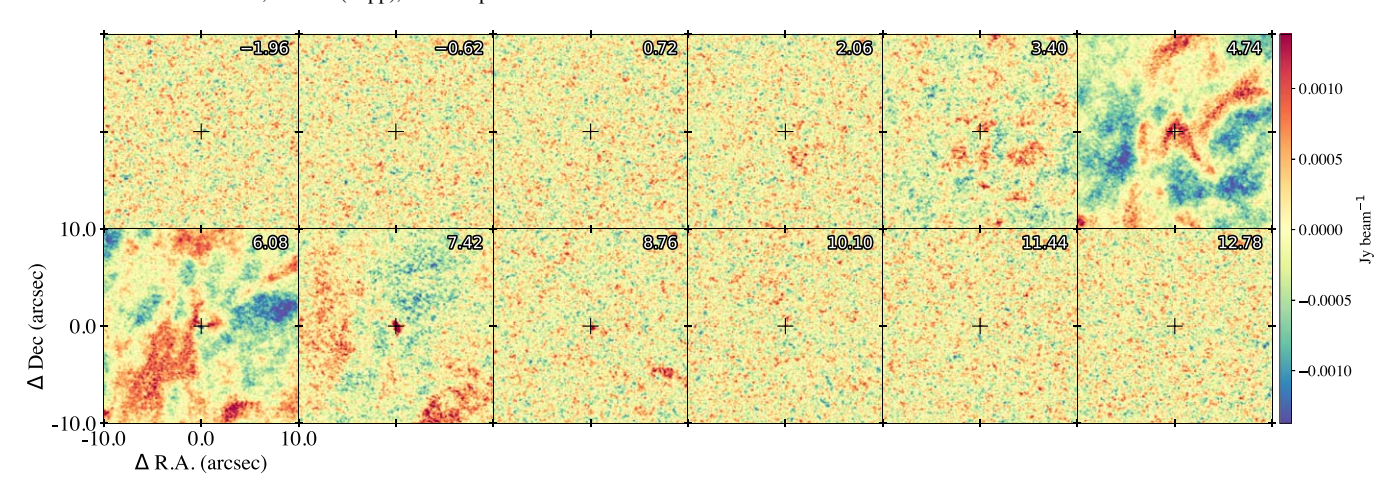


Figure A4. Same as Figure A1, but for $H_2CO(3_{0,3}-2_{0,2})$.

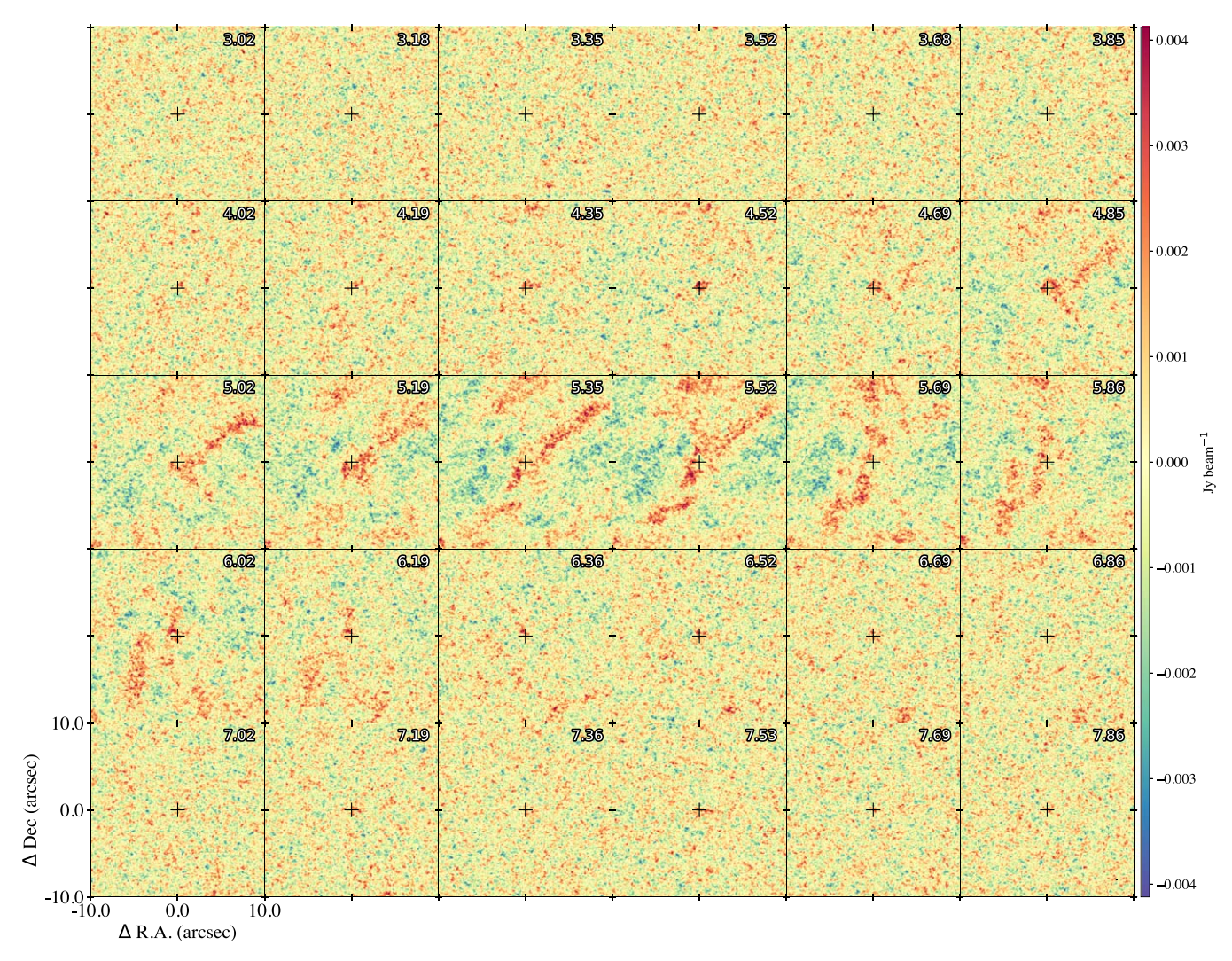


Figure A5. Same as Figure A1, but for $H_2CO(3_{2,1}-2_{2,0})$.

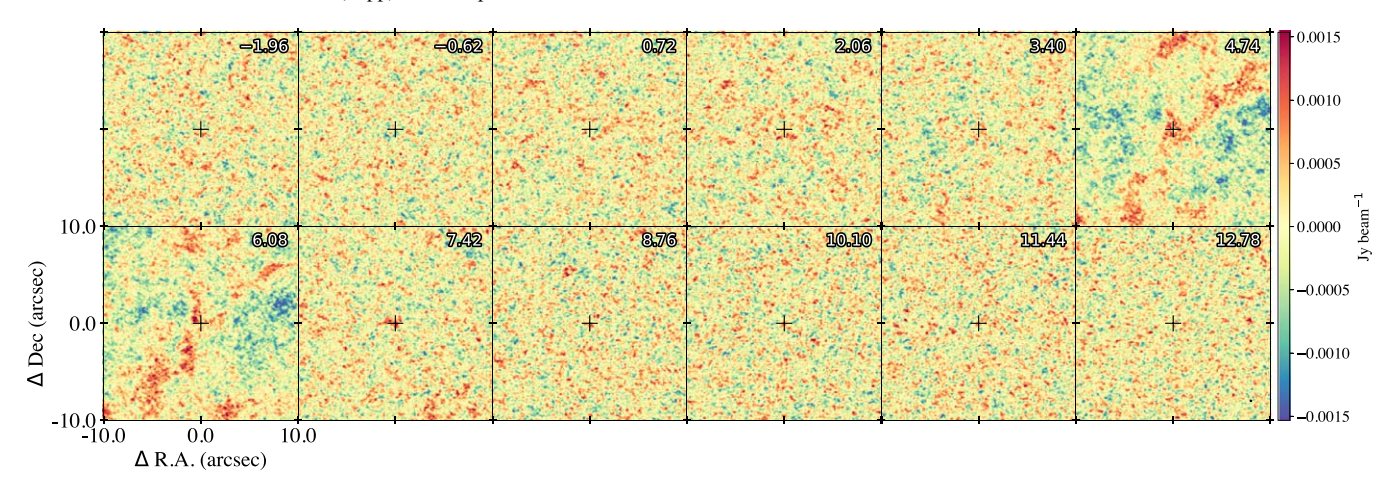


Figure A6. Same as Figure A1, but for $H_2CO(3_{2,2}-2_{2,1})$.

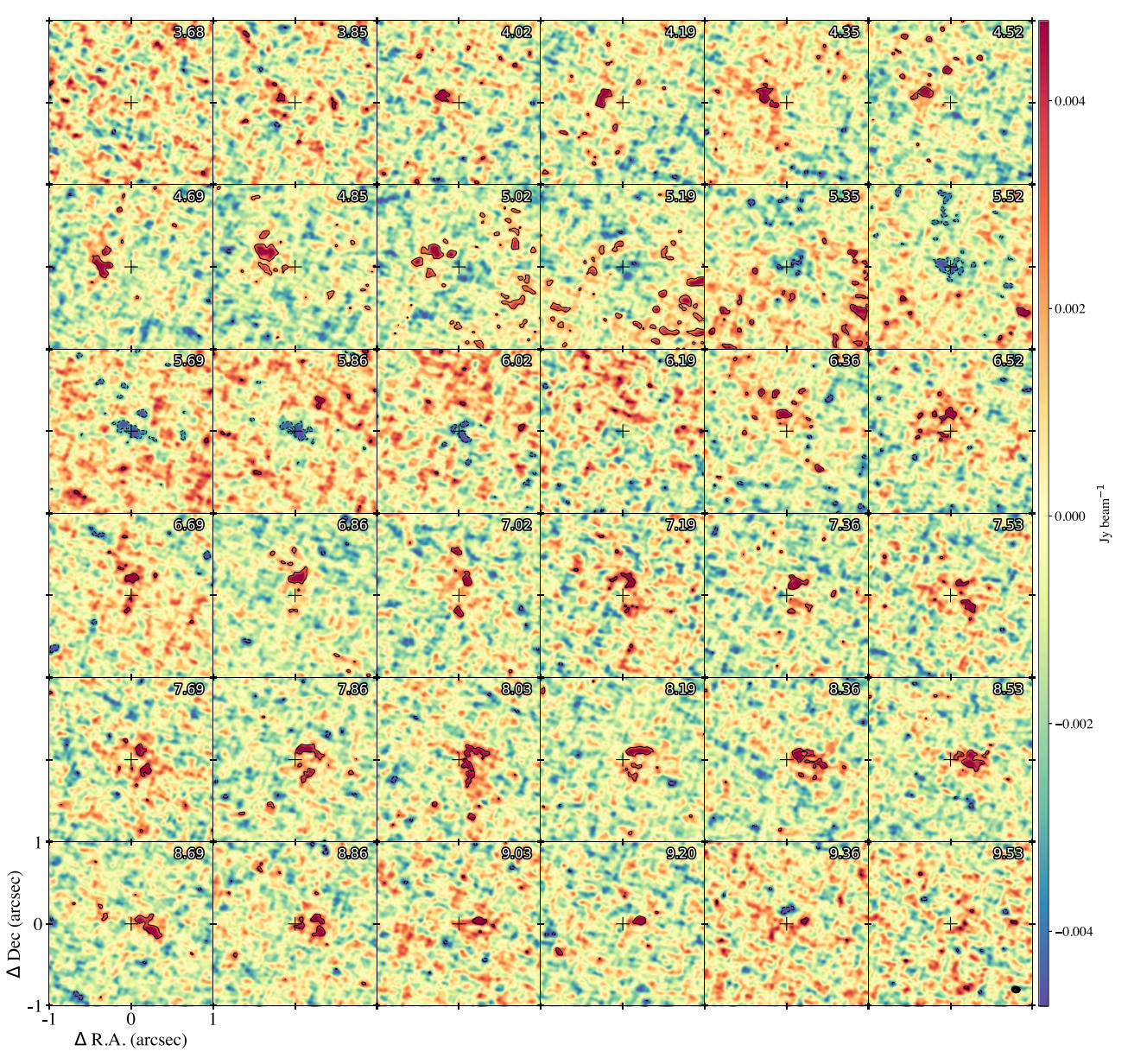


Figure A7. Channel maps showing the zoomed-in view of the $C^{18}O$ (2–1) emission around IRS5N. The numbers at the top show the corresponding velocity of each channel map. The solid contours represent the 3σ level, and the dashed lines show the -3σ level. The cross shows the peak position of the IRS5N continuum. The synthesized beam is shown in black in the bottom right corner of the final channel.

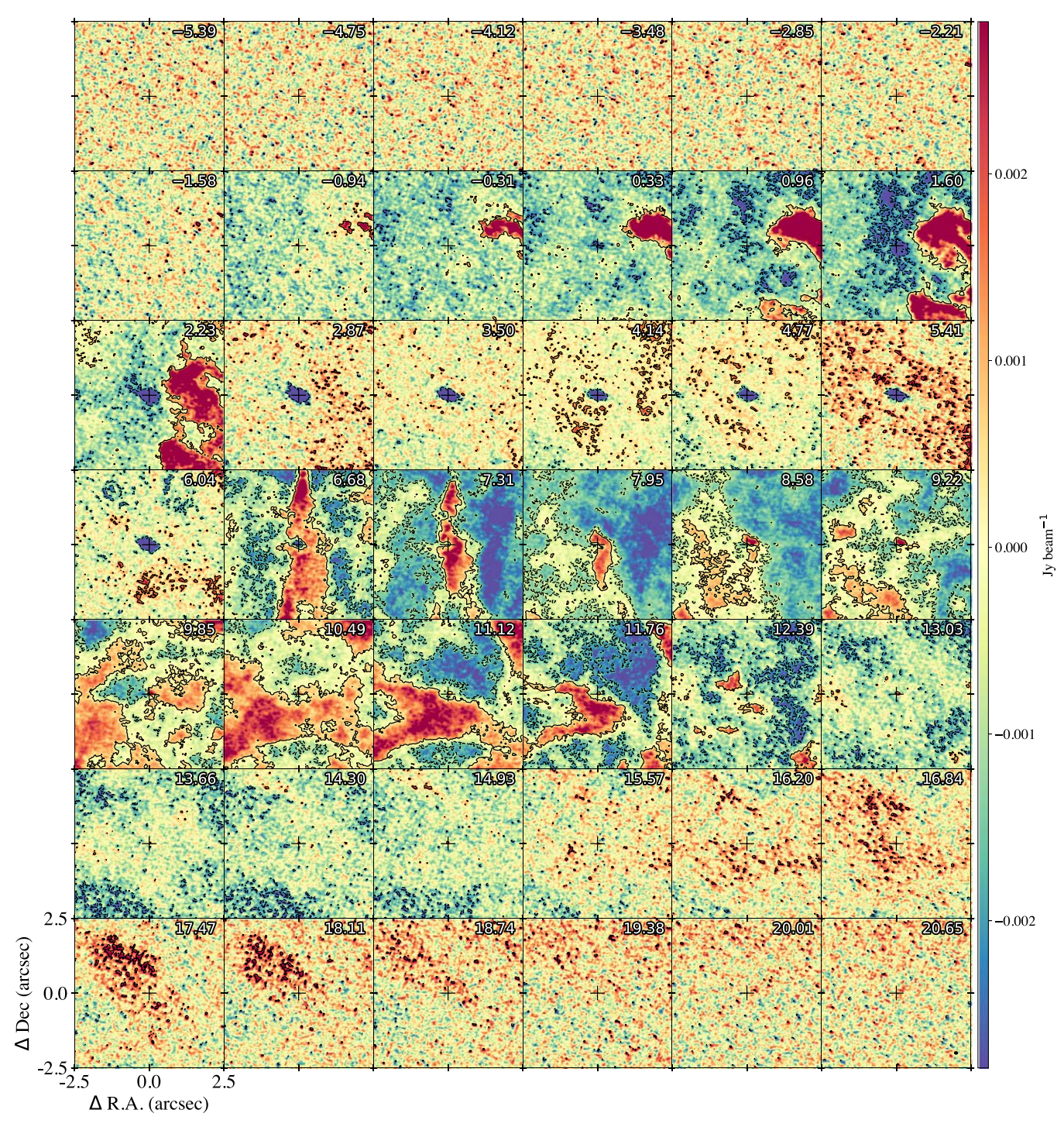


Figure A8. Same as Figure A7, but for ¹²CO (2–1).

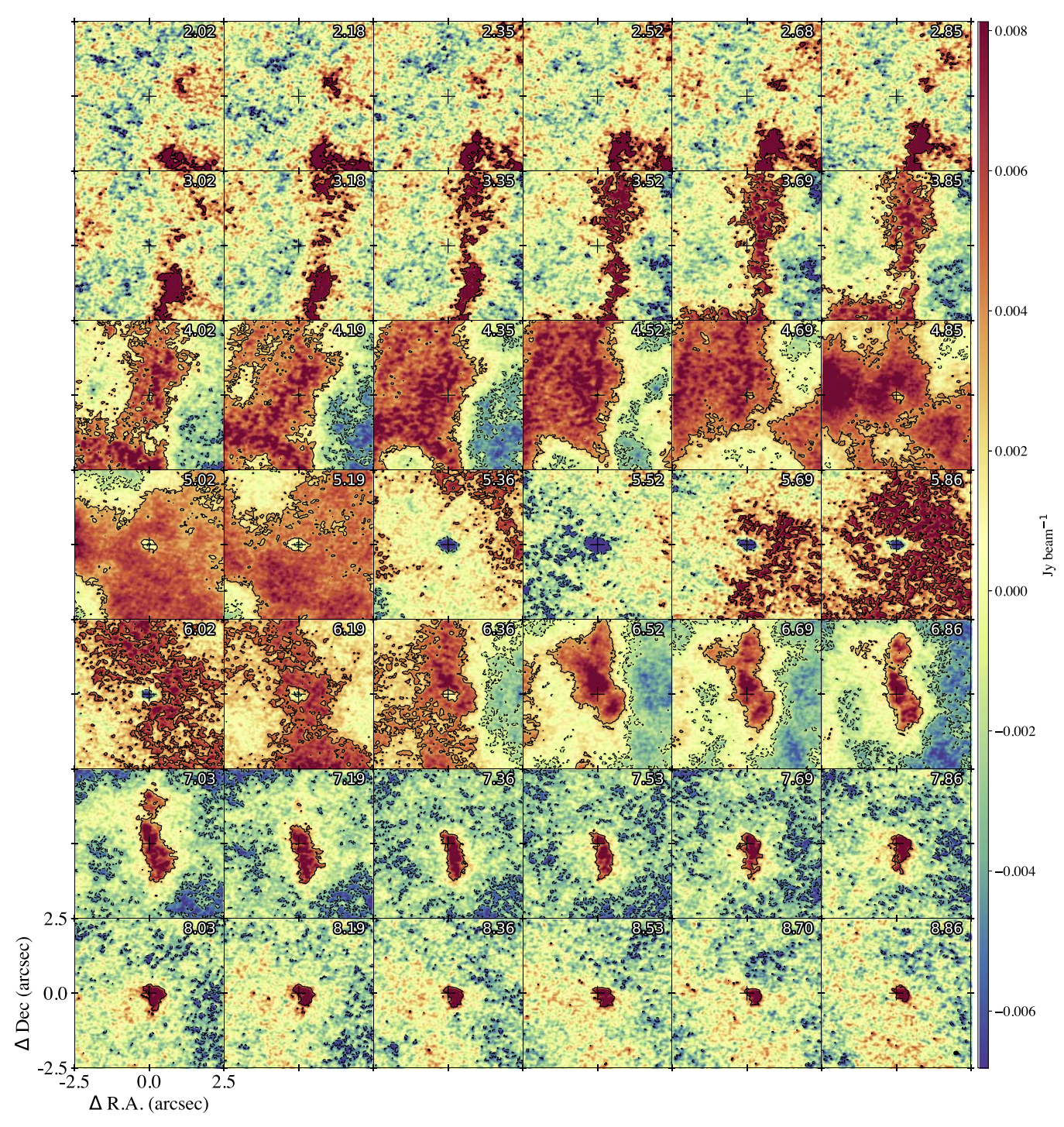


Figure A9. Same as Figure A7, but for ¹³CO (2–1).

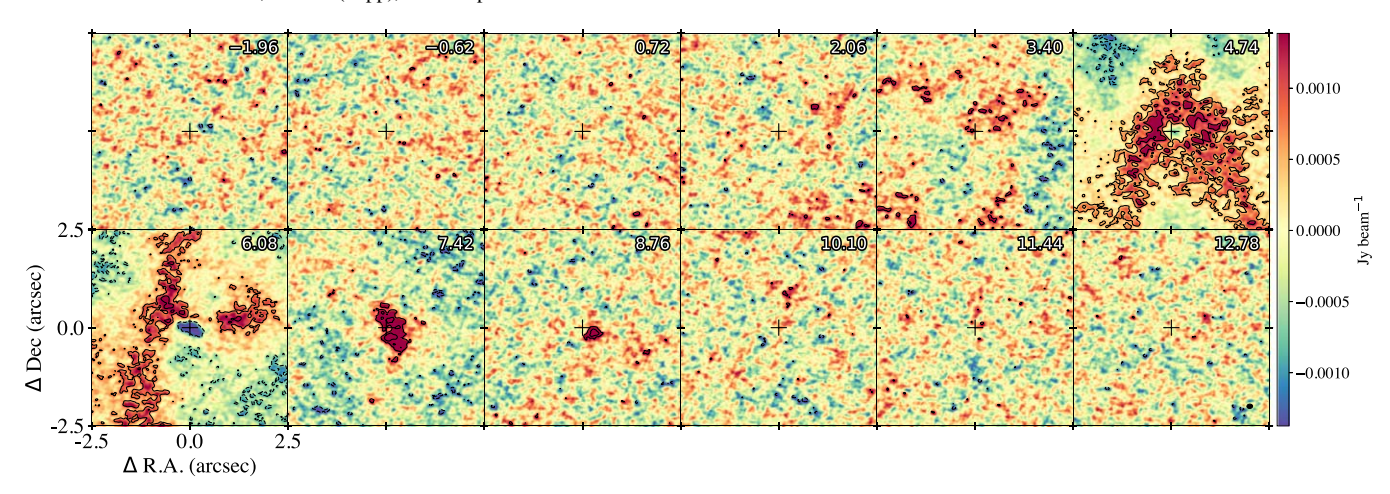


Figure A10. Same as Figure A7, but for $H_2CO(3_{0,3}-2_{0,2})$.

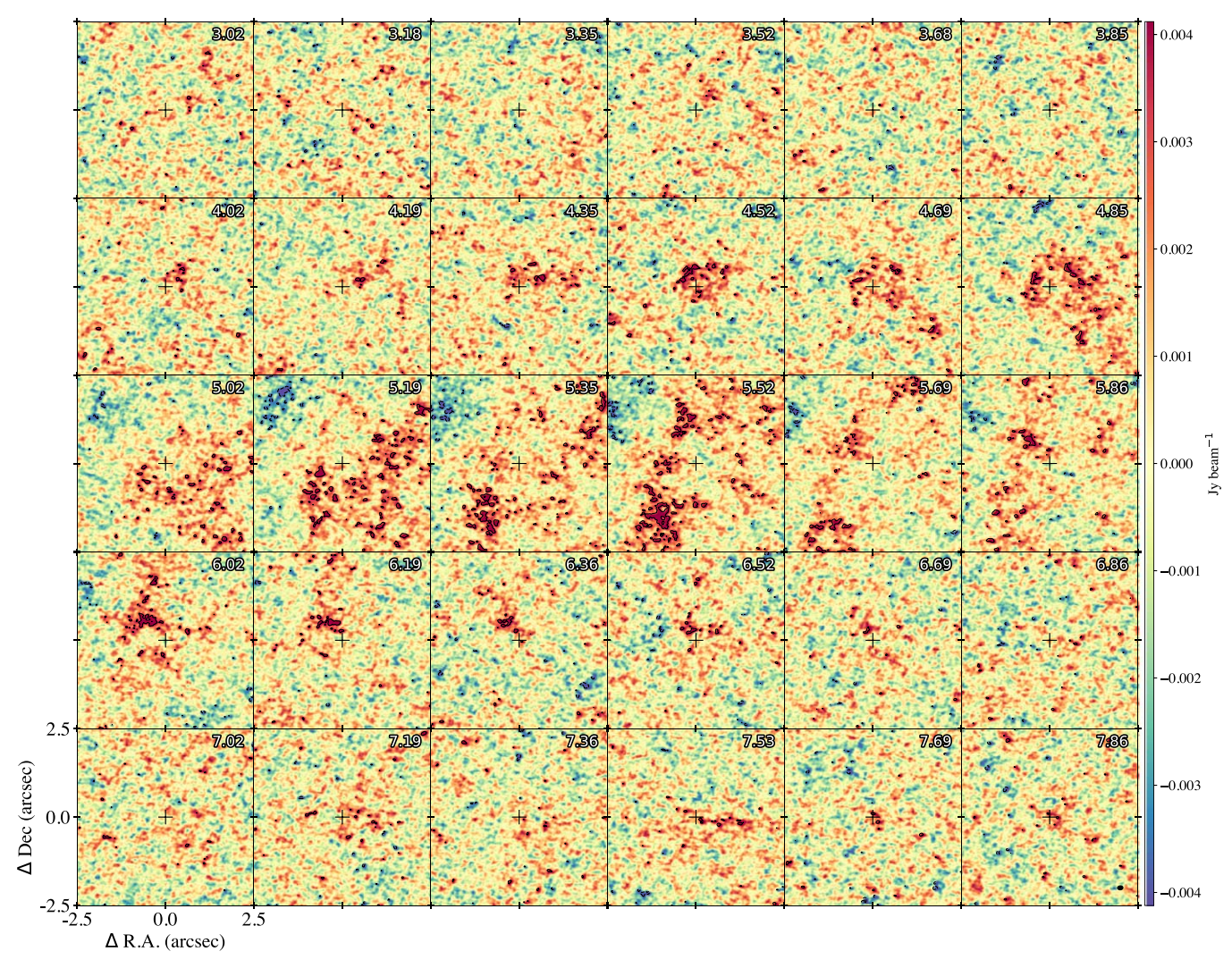


Figure A11. Same as Figure A7, but for $H_2CO(3_{2,1}-2_{2,0})$.

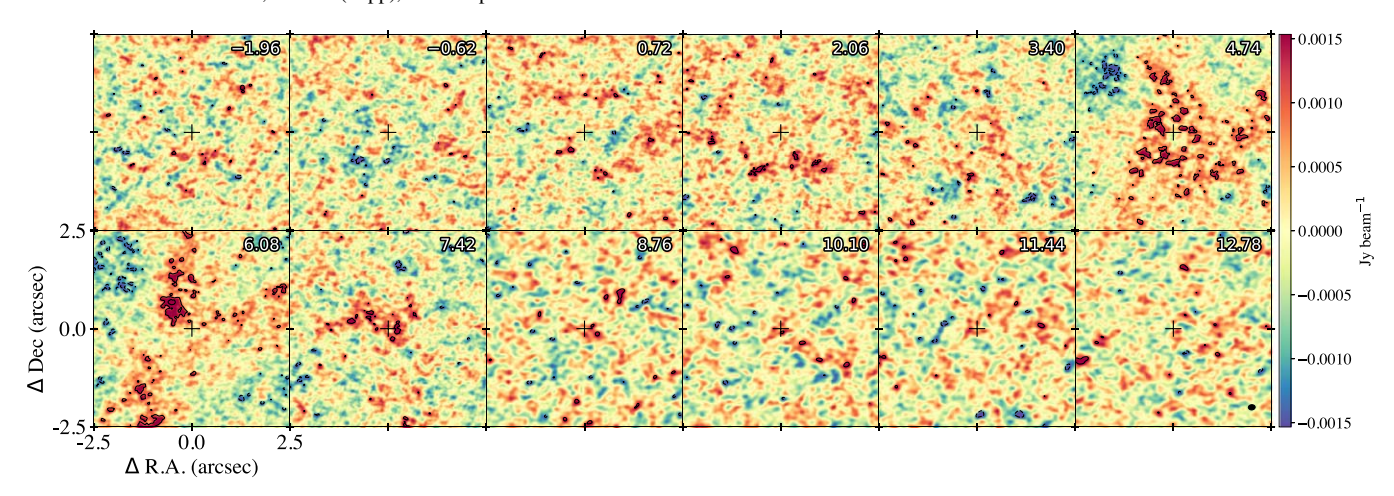


Figure A12. Same as Figure A7, but for $H_2CO(3_{2,2}-2_{2,1})$.

ORCID iDs

Chang Won Lee https://orcid.org/0000-0002-3179-6334 Jinshi Sai (Insa Choi) https://orcid.org/0000-0003-4361-5577

Woojin Kwon https://orcid.org/0000-0003-4022-4132 Itziar de Gregorio-Monsalvo https://orcid.org/0000-0003-4518-407X

Alejandro Santamaría-Miranda https://orcid.org/0000-0001-6267-2820

Hsi-Wei Yen https://orcid.org/0000-0003-1412-893X Yuri Aikawa https://orcid.org/0000-0003-3283-6884 Yusuke Aso https://orcid.org/0000-0002-8238-7709 Shih-Ping Lai https://orcid.org/0000-0001-5522-486X Jeong-Eun Lee https://orcid.org/0000-0003-3119-2087 Leslie W. Looney https://orcid.org/0000-0002-4540-6587 Nguyen Thi Phuong https://orcid.org/0000-0002-4372-5509

Travis J. Thieme https://orcid.org/0000-0003-0334-1583 Jonathan P. Williams https://orcid.org/0000-0001-5058-695X

References

ALMA Partnership, Brogan, C. L., & Pérez, L. M. 2015, ApJL, 808, L3
Andrews, S. M., Huang, J., Pérez, L. M., et al. 2018, ApJL, 869, L41
Andrews, S. M., & Williams, J. P. 2005, ApJ, 631, 1134
Ansdell, M., Williams, J. P., van der Marel, N., et al. 2016, ApJ, 828, 46
Aso, Y., & Sai, J. 2023, jinshisai/SLAM: First Release of SLAM, v1.0.0, Zenodo, doi:10.5281/zenodo.7783868
Astropy Collaboration, Price-Whelan, A. M., Sipőcz, B. M., et al. 2018, AJ, 156, 123
Beckwith, S. V. W., Sargent, A. I., Chini, R. S., & Guesten, R. 1990, AJ, 99, 924
Benisty, M., Bae, J., Facchini, S., et al. 2021, ApJL, 916, L2
Brinch, C., & Jørgensen, J. K. 2013, A&A, 559, A82
Busch, L. A., Belloche, A., Cabrit, S., Hennebelle, P., & Commerçon, B. 2020, A&A, 633, A126

```
Chen, W. P., & Graham, J. A. 1993, ApJ, 409, 319
Chiang, E. I., & Goldreich, P. 1997, ApJ, 490, 368
Chini, R., Kämpgen, K., Reipurth, B., et al. 2003, A&A, 409, 235
Cieza, L. A., González-Ruilova, C., Hales, A. S., et al. 2021, MNRAS,
   501, 2934
Commerçon, B., Launhardt, R., Dullemond, C., & Henning, T. 2012, A&A,
Dong, R., Zhu, Z., & Whitney, B. 2015, ApJ, 809, 93
Dutta, S., Lee, C.-F., Hirano, N., et al. 2022, ApJ, 931, 130
Galli, P. A. B., Bouy, H., Olivares, J., et al. 2020, A&A, 643, A148
Gonzalez, J. F., Laibe, G., & Maddison, S. T. 2017, MNRAS, 467, 1984
Harju, J., Haikala, L. K., Mattila, K., et al. 1993, A&A, 278, 569
Harris, C. R., Millman, K. J., van der Walt, S. J., et al. 2020, Natur, 585, 357
Huang, J., Andrews, S. M., Dullemond, C. P., et al. 2018, ApJL, 869, L42
Hunter, J. D. 2007, CSE, 9, 90
Isella, A., Benisty, M., Teague, R., et al. 2019, ApJL, 879, L25
Jørgensen, J. K., Kuruwita, R. L., Harsono, D., et al. 2022, Natur, 606, 272
Jørgensen, J. K., Schöier, F. L., & van Dishoeck, E. F. 2002, A&A, 389, 908
Jørgensen, J. K., Visser, R., Williams, J. P., & Bergin, E. A. 2015, A&A,
  579, A23
Keppler, M., Benisty, M., Müller, A., et al. 2018, A&A, 617, A44
Kratter, K., & Lodato, G. 2016, ARA&A, 54, 271
Kristensen, L. E., van Dishoeck, E. F., Bergin, E. A., et al. 2012, A&A,
Kuffmeier, M., Calcutt, H., & Kristensen, L. E. 2019, A&A, 628, A112
Kusaka, T., Nakano, T., & Hayashi, C. 1970, PThPh, 44, 1580
Lindberg, J. E., Jørgensen, J. K., Green, J. D., et al. 2014, A&A, 565, A29
Maret, S., Maury, A. J., Belloche, A., et al. 2020, A&A, 635, A15
Maureira, M. J., Arce, H. G., Dunham, M. M., et al. 2020, MNRAS, 499, 4394
McKee, C. F., & Ostriker, E. C. 2007, ARA&A, 45, 565
McMullin, J. P., Waters, B., Schiebel, D., Young, W., & Golap, K. 2007, in
   ASP Conf. Ser. 376, Astronomical Data Analysis Software and Systems
  XVI, ed. R. A. Shaw, F. Hill, & D. J. Bell (San Francisco, CA: ASP), 127
Neuhäuser, R., & Forbrich, J. 2008, in Handbook of Star Forming Regions,
   Volume II, ed. B. Reipurth, Vol. 5 (San Francisco, CA: ASP), 735
Nisini, B., Antoniucci, S., Giannini, T., & Lorenzetti, D. 2005, A&A, 429, 543
Nutter, D. J., Ward-Thompson, D., & André, P. 2005, MNRAS, 357, 975
Ohashi, N., Saigo, K., Aso, Y., et al. 2014, ApJ, 796, 131
Ohashi, N., Tobin, J. J., Jørgensen, J. K., et al. 2023, ApJ, 951, 8
Peterson, D. E. 2011, ApJS, 194, 43
Robitaille, T. 2019, APLpy v2.0: The Astronomical Plotting Library in Python,
   doi:10.5281/zenodo.2567476
RobitailleT., & BressertE. (2012) APLpy: Astronomical Plotting Library in
  Python, Astrophysics Source Code Libraryascl:1208.017
Sadavoy, S. I., Myers, P. C., Stephens, I. W., et al. 2018, ApJ, 869, 115
Sakai, N., Sakai, T., Hirota, T., et al. 2014, Natur, 507, 78
Sandell, G., Reipurth, B., Vacca, W. D., & Bajaj, N. S. 2021, ApJ, 920, 7
Schilke, P., & Walmsley, C. M. 1997, A&A, 321, 293
Segura-Cox, D. M., Schmiedeke, A., Pineda, J. E., et al. 2020, Natur, 586, 228
Sharma, R., Tobin, J. J., Sheehan, P. D., et al. 2020, ApJ, 904, 78
Sheehan, P. D., & Eisner, J. A. 2017, ApJ, 851, 45
Sheehan, P. D., Tobin, J. J., Federman, S., Megeath, S. T., & Looney, L. W.
```

2020, ApJ, 902, 141

```
Simon, M., Dutrey, A., & Guilloteau, S. 2000, ApJ, 545, 1034
Taylor, K. N. R., & Storey, J. W. V. 1984, MNRAS, 209, 5P
Terebey, S., Shu, F. H., & Cassen, P. 1984, ApJ, 286, 529
Testi, L., Birnstiel, T., Ricci, L., et al. 2014, in Protostars and Planets VI, ed.
H. Beuther et al. (Tucson, AZ: Univ. Arizona Press), 339
Tobin, J. J., Hartmann, L., Chiang, H.-F., et al. 2012, Natur, 492, 83
Tobin, J. J., Kratter, K. M., Persson, M. V., et al. 2016, Natur, 538, 483
Tobin, J. J., Sheehan, P. D., Megeath, S. T., et al. 2020, ApJ, 890, 130
Tomida, K., Okuzumi, S., & Machida, M. N. 2015, ApJ, 801, 117
```

```
Tychoniec, Ł., Manara, C. F., Rosotti, G. P., et al. 2020, A&A, 640, A19 van der Wiel, M. H. D., Jacobsen, S. K., Jørgensen, J. K., et al. 2019, A&A, 626, A93

Wakelam, V., Ceccarelli, C., Castets, A., et al. 2005, A&A, 437, 149

Wang, H., Mundt, R., Henning, T., & Apai, D. 2004, ApJ, 617, 1191

Zhang, K., Blake, G. A., & Bergin, E. A. 2015, ApJL, 806, L7

Zhang, S., Zhu, Z., Huang, J., et al. 2018, ApJL, 869, L47

Zucker, C., Speagle, Joshua, S., Schlafly, Edward, F., et al. 2020, A&A, 633, A51
```